# Flow and Heat Transfer in a Crossflow past a Circular Tube placed in a Channel
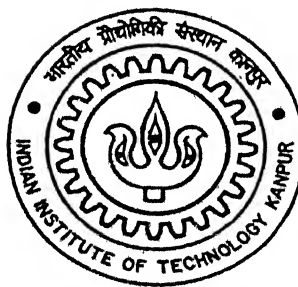
by
## SUDIPTA BASU

**DEPARTMENT OF MECHANICAL ENGINEERING**
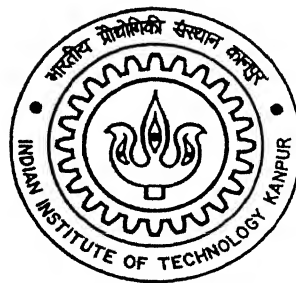**INDIAN INSTITUTE OF TECHNOLOGY KANPUR**
February, 2001

# Flow and Heat Transfer in a Crossflow past a Circular Tube placed in a Channel

*A Thesis Submitted*
*in partial Fulfillment of the requirements*
*for the Degree of*

**MASTER OF TECHNOLOGY**

by
**SUDIPTA BASU**

**DEPARTMENT OF MECHANICAL ENGINEERING**
**INDIAN INSTITUTE OF TECHNOLOGY KANPUR**
**February, 2001**

# Certificate

This is to certify that the thesis entitled **"Flow and Heat Transfer in a Crossflow past a Circular Tube placed in a Channel"** by Mr. Sudipta Basu has been carried out under my supervision. The contents of this thesis have not been submitted to any other Institute or University for the award of any degree and diploma.

<div align="right">

*Gautam Biswas*

Dr. Gautam Biswas

Professor

Department of Mechanical Engineering

Indian Institute of Technology

Kanpur-208016

</div>

February 28, 2001

# Abstract

Numerical investigation of flow and heat transfer in a rectangular duct with a built-in circular tube has been carried out for a Reynolds number of 1000 and blockage ratio of 0.44. A finite volume discretization method due to Eswaran and Prakash (1998) and a SMAC (Harlow and Amsden, 1970) based solution algorithm have been applied to solve the governing differential equations. Since the heat transfer in the duct is dictated by the flow structure, the present study is directed toward characterization of the flow structure. To this end, the topological theory shows the promise of becoming a powerful tool for the study of the flow structure. Computations show the helical vortex tubes in the wake and existence of the horseshoe vortex system. The $w$ component of velocity is surprisingly very large in front and in the near wake of the tube. The qualitative analyses of the limiting streamlines on the tube and the bottom-plate reveal the existence of a complex flow field. The separation lines as well as singularity points (saddle and nodal points) have been investigated. The iso-Nusselt number contours and the span-averaged Nusselt number in the flow passage draws an insightful conclusion about the heat transfer performance in the duct.

# Acknowledgements

At the outset, I would like to express my heartfelt gratitude to my thesis supervisor Dr. Gautam Biswas for his invaluable help, constant encouragement and sagacious advice throughout my M.Tech. program. His effective guidance, dynamism, coupled with his clarity of thoughts has directed the work toward completion. I feel very fortunate to have the opportunity to work with him and I shall always remain obliged to his greatness in devoting a large share of his valuable time and knowledge to this work. It is not possible to express my full gratitude to him in the above few words.

I am especially thankful to Dr. Vinayak Eswaran for introducing me to the exciting field of Computational Fluid Dynamics. His excellent teaching and well-selected assignments in the CFD course developed the passion and aptitude for this subject.

I gratefully acknowledge the facilities received from the CFD lab. But for the ideal working environment of this lab. assiduously built by Prof. Gautam Biswas , my thesis work could not have been completed in time.

I would like to thank all my colleagues at the CFD lab. for their help and cooperation. Vivek, Srinivas, Shaligram, Deepti, Tomar, Ajay, Vishwadeep, Neetu all deserve acknowledgement. Special thanks to Vivek for his invaluable help regarding post-processing works.

The silent support, inspiration, good wishes and blessings of my parents have been really indispensable.

I shall be always grateful to those invisible persons whose support cannot be expressed in words.

<div align="right">Sudipta.Basu</div>

# Contents

# List of Figures

# Nomenclature

B      channel width

$C_p$    Pressure Coefficient, $(p - p_\infty)/\frac{1}{2}\rho u_\infty^2$

cv     Control Volume

D      diameter of the cylinder

F      Mass flux through a cell face

H      channel height

K      Thermal Conductivity

Nu    Local Nusselt number, $\dfrac{\partial \theta}{\partial y}$

p      Static Pressure

P      Grid Control Function

Q      Grid control Function

Re     Reynolds number based on channel height $(\rho u_{av} H)/\mu$

S      Surface area of a cell face

t      time

u      axial velocity

v      spanwise velocity

w      normal or vertical velocity

x      axial dimension of coordinates

y      Spanwise dimension of coordinates

z      normal or vertical dimension of coordinates

T      Temperature

## Greek Letters

$\gamma$    Upwinding factor

$\alpha$    Thermal diffusivity

$\rho$    Density of the fluid

$\theta$    Nondimensional temperature $(T - T\ )/(T_w - T_\infty)$

$\xi, \eta$    Coordinates in computational space

## Subscripts

j    Cell face

## Superscripts

n,   n + 1    time level

# Chapter 1

# Introduction

## 1.1    Description of the Problem

Fin-tubes are commonly used in the gas-liquid crossflow heat exchangers, where the gas generally flows across the tubes and the liquid flows inside the tubes. Figure 1.1 shows a schematic diagram of the core region of a fin-tube heat exchanger. The purpose of the fin is to enhance the heat transfer rate on the gas side, since the transport coefficient on the gas side is usually smaller than the liquid side. Numerical investigation on the related topic has been reported earlier by Biswas, Mitra and Fiebig (1994). In the above investigation the enhancement of heat transfer from the fin surfaces is achieved by inducing longitudinal streamwise vortices in the flow field. The longitudinal vortices are generated by placing delta-winglet type vortex generators on the flat surface (Figure 1.2). The longitudinal vortices developed along the side edge of the delta-winglets due to the pressure difference between the front surface facing the flow and the back surface. The longitudinal vortices are so called the streamwise vortices since the axes of the vortices are aligned to the flow direction. The streamwise vortices interact with an otherwise two-dimensional boundary layer and produce a three-dimensional swirling flow that mixes near wall fluid with the free stream. This mechanism strongly enhances the entrainment of fluid from the periphery to the core region of the flow field. Thus the thermal boundary

# Fin Tube Heat Exchanger

**Liquid**

Tube

Fins

Gas
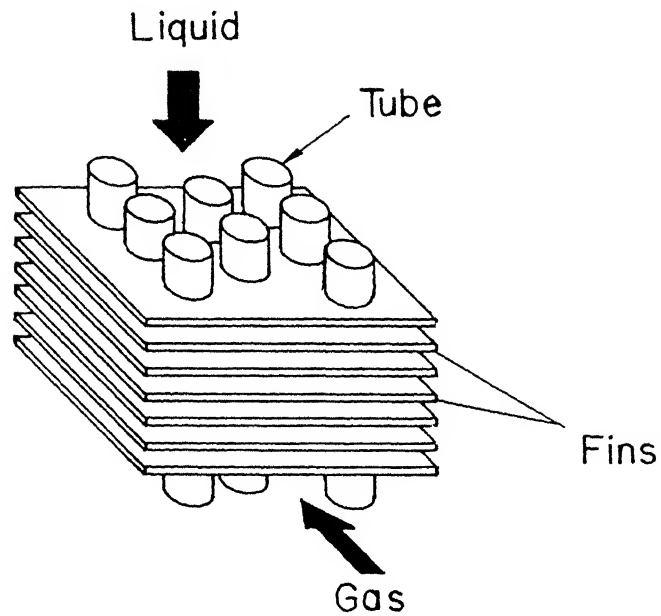
Schematic Diagram of Core Region of a Fin-Tube Heat Exchanger.
Figure 1.1

$\beta$ : angle of attack

$b/2$

$$S = \frac{1}{2} bl$$

$$\Lambda = b^2/S$$

Winglet pair
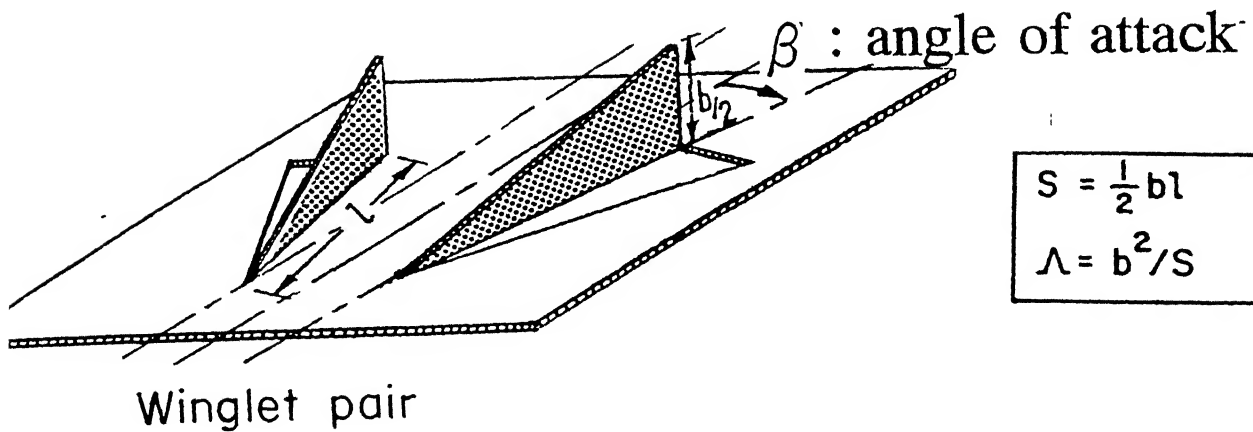
Delta-Winglet Type Vortex Generators on Flat Surface
Figure 1.2

layer is disrupted and the heat transfer rate is enhanced. The additional pressure losses are modest because the form drag for such winglet-type slender bodies is low.

The air-cooled condenser of geothermal plants consists basically of the same fin-tube arrangement as shown in Figure 1.1. Air is forced through several rows of this fin tubes by large fans. The condenser units can be very large, consuming a large fraction of the overall capital cost of these plants. In addition the power required to operate the fans represents a significant parasitic house load, reducing the net power production of the plant. In order to analyze the mechanisms involved in the heat transfer and flow behavior in such heat exchangers, a detailed investigation on a heat exchanger module is necessary. Such a module is shown in Figure 1.3.

# 1.2 The Scope of the Present Work

The main aim of the research is to prescribe the heat transfer enhancement strategies of the air-cooled condensers for the geothermal plants. In order to achieve this desired objective a detailed three-dimensional numerical model has been formulated to provide a better understanding of the flow physics. In the numerical model, the full Navier-Stokes equations together with governing equations of energy are solved in a rectangular channel with a built in circular cylinder (Figure 1.3). A detailed analysis of the flow structure along with heat transfer characteristics in such a module is studied, as it is crucial for design of high-performance heat exchangers.

no-slip topwall

sidewall

H

no-slip bottomwall

Temperature $T_w$

D

$T_w$

$v = 0$ $w = 0$

Temperature $T_\infty$

no-slip bottomwall

z,w
x,u
y,v

$u = u(z)$
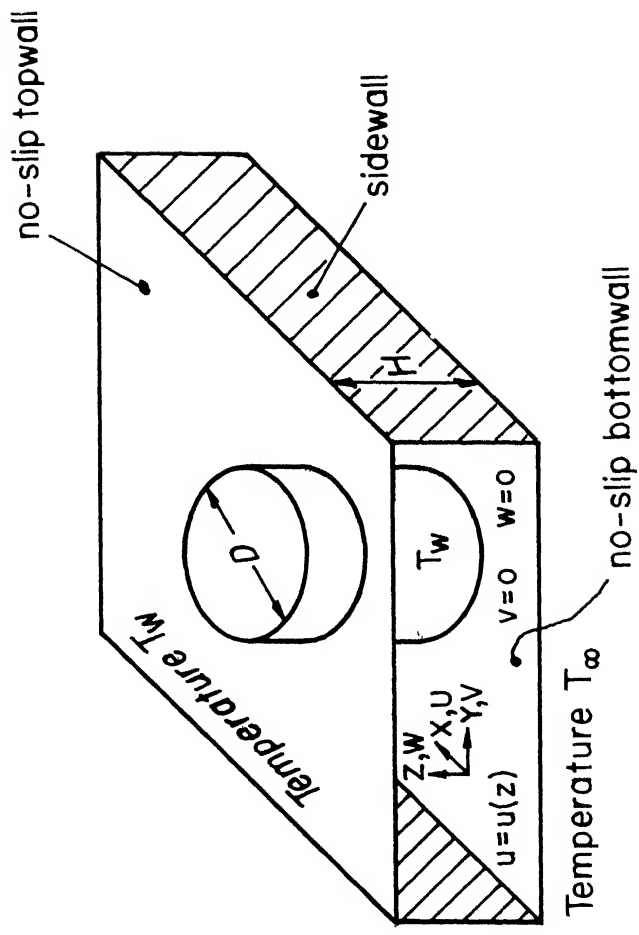
Heat Exchanger Module
Figure 1.3

## 1.3 Layout of the Thesis

In Chapter-1, we have already discussed the genesis of the problem. Chapter-2 of the thesis provides a review of literature relevant to the basic mechanisms involved in augmentation of heat transfer and the algorithms related to solving the Navier-Stokes equations. A concise review of modeling aspects of turbulent flow has also been focussed in this chapter. The mathematical formulation of the problem for simulation is presented in chapter-3. In this chapter, the geometry, the governing equations, boundary conditions and the grid generation techniques are described. Chapter-4 deals with the solution algorithm. In this chapter, the discretization schemes and the solution procedure using control volume formulation are described in detail. Chapter-5 discusses results for laminar flow. In this chapter, a detailed study of flow physics and associated heat transfer characteristics are presented. Chapter-6 includes the concluding remarks and the scope for further research.

# Chapter 2

# Literature Survey

## 2.1 Introduction

The objectives of present study have been briefly outlined in the previous chapter. A variety of experimental and considerable amount of analytical and computational research have been carried out on the enhancement of heat transfer. Especially the enhancement of heat transfer through manipulation of surface geometry has been analyzed by many researchers and practitioners since the earliest documented studies of heat transfer. In this chapter a survey of the relevant literature is presented to indicate the extent of work already reported in open literature pertaining to the enhancement of heat transfer by using surface-mounted protrusions. In order to analyze the flow structure and heat transfer in such applications, a detailed computational study is needed. The flow regime for such applications can be both laminar and turbulent. In the present literature review the attention is also focussed, on important numerical techniques developed in the recent past for solving the conservation equation for complex flows and heat transfer. Although the numerical solution of the governing conservation equations for laminar flows has become a realizable goal, the solution for turbulent flows even for simple geometry is indeed a formidable task. The relevant literature on turbulence modeling has been looked into in brief with

the intent to understand various modeling and computational strategies. This survey helps in suggesting the work that should be carried out to accomplish the objectives enumerated in the earlier chapter. The literature is reviewed from three different viewpoints. In the first section, an overview of the work done by various researchers in the area of augmentation of heat transfer is presented and discussed. The second section presents a review of investigations pertaining to the numerical methods with regard to the task of computing flow fields in complex geometries. Basically, this section deals with available scheme for solving the complete Navier-stokes equations. In the third section a brief review on modeling aspects of turbulent flow has been presented.

## 2.2   Fin-Tube Heat Exchangers

As it was mentioned in the previous chapter that our primary interest is to enhance the heat transfer in the gas side of fin-tube heat exchangers (with flat fins) and enhancement of heat transfer in fin-plate heat exchangers. With this intent, we would like to study different investigations related to augmentation of heat transfer suitable for the applications enumerated earlier.

Augmentation of heat transfer is of special interest in channel flows where the rate of heat transfer between the fluid and channel walls deteriorates as the boundary layer grows on the channel walls and the flow tends to become fully developed. Protrusions can be mounted on these channel walls in order

to disturb the growth of boundary layer and thereby enhance the heat transfer between the flowing fluid and channel walls. Two relevant applications using such flow configurations are the heat transfer between the gas and the fin in the case of gas-liquid fin-tube crossflow heat exchangers and the heat transfer between the flowing fluid and plates in the case of fin-plate heat exchangers. The evolution towards a fully developed flow can be disturbed by using a multi-louvered surface geometry for plates. Investigation by Achaichia and Cowell (1988) provides a detailed performance data for louvered fin surfaces. However in using louvered fins, enhancement is obtained at the price of high-pressure drop. To circumvent this difficulty, protrusions in the form of slender delta-wings or winglets can be deployed (Figure 1.2). As shown, the base of the wing remains attached to the fin and the apex faces the incoming stream with an angle of attack with this configuration. The longitudinal vortices are generated along the side edge of the wing-shaped vortex generator due to the pressure difference between the front surface facing the flow and the back surface. These longitudinal vortices, generated by the vortex generators, can be made to disturb the growth of boundary layer in a channel by exchanging the fluid from the near-wall-region with the channel-core-region and thus they can serve to enhance the heat transfer rate while producing less increase in pressure penalty. Use of longitudinal vortices for boundary control is well known (Pearcey, 1961) and the vortex generators are used in commercial airplanes for this purpose.

Formation of streamwise longitudinal vortices behind a slender aerodynamic object is a research topic of considerable interest for several years. Both the theoretical and experimental investigations on flow past a delta wing have been conducted and reported in literature by number of researchers. Hummel and Srinivasan (1967) have made important contribution in revealing the complex flow structure behind a delta wing. They have conducted experiments and presented pressure distribution and vortex structure of the flow around a delta wing of unit aspect ratio with an angle of attack of 20°.

Thomas et al. (1990) have computed low-speed laminar flow over a low aspect ratio delta wing up to 40° angle of attack using an upwind biased finite volume algorithm. The differencing schemes used are second-order accurate and a multigrid algorithm is employed to promote convergence to steady state. The predicted results and lift coefficient have remarkable agreement with experiments due to Hummel (1973). At 40° angle of attack, a bubble-type vortex breakdown is evident in the computations.

Experimental investigations due to Fiebig et al. (1986), Fiebig et al. (1991) and Tiggelbeck et al. (1992) can be referred to in connection with augmentation of heat transfer by means of longitudinal vortices. Experimental investigation due to Fiebig et al. (1986) is the first systematic study to compare the performance of different kinds of vortex generators viz., delta wing, rectangular wing, delta winglet pair and rectangular winglet pair in the Reynolds number range of 1360 and 2270. Their observation

depicts that the delta wing is the best vortex generator from the heat transfer point of view. Another important feature of their observation is that the heat transfer coefficient increases with the increase in angle of attack till the vortex breakdown takes place. Tiggelbeck et al. (1992) used multiple rows of vortex generators in an aligned arrangement within a channel and observed their influence on flow structure. The flow structure in the wake of the second row is qualitatively similar to that of the first row. Their flow visualization by a laser light shift technique has revealed that the concentrated vortex pair generated by a small aspect ratio delta wing at large angle of attack has elliptic shape due to the influence of channel walls. They also observed that the peak value of the spanwise-averaged Nusselt number at the wake of second row is strongly dependent on the spacing between the two rows.

Computational studies on related topics have been performed by Fiebig et al. (1989) and Biswas and Chattopadhyay (1992) for laminar flow in geometrical configuration of delta wing placed inside a channel. Both studies have discussed the influence of angle of attack and Reynolds number on velocity and temperature fields.

It has been already discussed that the gas side heat transfer coefficient in a gas-liquid fin-tube crossflow heat exchanger is small compared to that of liquid side. The mechanism of heat transfer between the gas and the solid surfaces in such cases is to be understood in detail. Let us consider only one tube in a channel, formed by the two neighboring fins. The flow field

consists of a horseshoe vortex system, a dead water zone at the juncture of the tube and the plate and a von-Karman vortex street in the middle. In order to enhance heat transfer in such flow configuration, vortex generators can be mounted on the plates, which makes the flow field extremely complex. Dong (1989) and Valencia (1992) have conducted experimental investigation, to observe the influence of winglet type vortex generators in a channel with a built-in circular tube. Biswas et al. (1994) have observed that in the absence of the winglet-type vortex generators, relatively little heat transfer takes place in the downstream of the circular tube which is the recirculation region with low velocity. However, they observed an enhancement of heat transfer as high as 240 percent in the wake region behind the cylinder in the presence of winglet-type longitudinal vortex generators. Fiebig et al. (1994) have studied in detail the conjugate heat transfer of a fin-tube heat exchanger for three-dimensional thermally and hydrodynamically developing laminar flows. They have identified an unique heat transfer phenomenon, a directional reversal of heat transfer (HTR) occurred locally on the fin in the tube wake for large Reynolds number and a small fin efficiency parameter, Fi (ratio of fin to fluid conductivity times fin thickness to fin pitch).

Recently computational studies have been extended to periodic configurations, which are realistic in terms of plate-fin exchangers with perforated fins or slotted channels. Heat transfer surfaces periodically interrupted along the streamwise direction have been widely used in order to obtain improved performance of the heat exchanger devices. Such an arrangement maybe viewed as a succession of collinear plate-segments

aligned parallel to flow with slots between successive plates. Each slot enables the interruption of thermal boundary layer where the highest resistance to heat flux occurs and a new boundary layer with lower thermal resistance begins. It also allows a very good mixing of flow with self-sustained oscillation when the system is operating above the critical conditions (Reynolds number). The channels, which have such operating conditions, have been classified as communicating channels. As it has been said, above a critical value of Reynolds number (much within the laminar region), the initial steady flow becomes unstable to small disturbances. At this instant the flow is said to have undergone a bifurcation from steady state to time periodic, and finally to self-sustaining oscillatory regime. Supercritical bifurcation and narrow band excitation characterize these flows (Ghaddar et al.1986 a; Ghaddar et al.1986 b; Amon and Patera 1989). Appreciable transport augmentation takes place in this range of Reynolds number (Majumdar and Amon, 1992).

Webb and Ramadhyani (1985) have analyzed fluid flow and heat transfer characteristics through a parallel plate channel with transverse ribs, which act as vortex generators. Significant heat transfer augmentation is obtained in their study. Acharya et al. (1991) explained vortex interaction between two such ribs in a channel for the sub harmonic excitation of shear layers. In a similar way a significant augmentation is obtained by positioning vortex generators at key locations in the flow (Myrum et al. 1992).

Many researchers have observed longitudinal vortices in various complex flow configurations. Naturally, the interaction of such vortices with boundary layer and its effect on heat transfer is a subject of interest to them. Some examples are Taylor–Görtler vortices in boundary layers on concave curved surfaces, the horseshoe vortices formed by an obstruction protruding from surface and wingtip vortices impinging on a downstream surface. The embedded vortex is capable of strongly perturbing the boundary layer and influencing the heat transfer characteristics. In addition, longitudinal vortices usually maintain their coherence over a long streamwise distance. As a consequence, the heat transfer effects behind the vortex generator are very persistent. Eibeck and Eaton (1987), Westphal and Mehta (1987) have worked extensively in this field with more focus to the turbulent boundary layer. Eibeck and Eaton (1987) have conducted experiments on longitudinal vortices embedded in a turbulent boundary layer and resultant heat transfer effects. Longitudinal vortices are found to influence heat transfer behavior significantly. Local Stanton number is increased is by as much as 24 percent resulting in a net increase in spanwise average heat transfer coefficient. Despite the presence of turbulent diffusion, the influence of longitudinal vortices on momentum and energy transport can be traced at a location as far downstream as 60 wing chords behind the delta wing.

## 2.3 Numerical Methods for Solving Navier–Stokes Equations

Different solution techniques for full Navier-Stokes equations have been developed during the past three decades. The major difficulty encountered during the solution of incompressible flows arises from the absence of any explicit equation for pressure and due to the nature of spatial coupling of the pressure and velocity. For incompressible flow problems, pressure does not have the usual thermodynamical meaning. Here it is a relative variable, which adjusts itself instantaneously for the condition of zero mass divergence to be satisfied at all computational cells. This behavior is related to the well-known fact that in an incompressible fluid the speed of the sound is infinite. As a consequence, the pressure field cannot be calculated by an explicit time advancement procedure, instead it requires at least a partially implicit determination which takes into account the coupling between the pressure and velocity fields as well as the effects the velocity boundary conditions. This aspect is the most distinctive feature of the primitive variable formulation of the incompressible Navier-Stokes equations.

The difficulty of determination of pressure field can be resolved in the stream fuction-vorticity approach. But the stream fuction-vorticity approach loses its attractiveness when the three-dimensional flow is computed because of the absence of a single scalar stream function in the three-dimensional space.

A three-dimensional problem demands a primitive variable approach. Efforts have been made so that two-dimensional as well as three-dimensional problems could be computed following a primitive variable approach without encountering non-physical wiggles in pressure distribution. As a remedy, it has been suggested to employ a different grid for each variable. Harlow and Welch (1965) have used such a staggered grid for the dependent variables in their well-known MAC (Marker and Cell) method. The MAC method of Harlow and Welch is one of the earliest and widely used explicit methods for solving the full Navier-Stokes equations. In this method, solutions of velocities are obtained using a two step procedure. In the first step called the predictor step, the provisional values of velocity components are computed explicitly using advection, diffusion and pressure gradients of the earlier time steps. This explicitly advanced provisional velocity field may not necessarily ensure a divergence free velocity field. Hence, in the second step called the corrector step, the pressure and velocity components are corrected so that the velocity field satisfies the continuity equation. This is done through the solution of a Poisson equation for pressure. A relative technique, known as pseudo-compressibility method, developed by Chorin (1967) involves a simultaneous iteration of the pressure and velocity components. Vicelli (1971) has shown that the method due to Chorin (1967) and the MAC method are equivalent.

The original version of MAC method has been modified by Harlow and Amsden, popularly known as Simplified MAC (SMAC, 1970), Nicholas and Hirt (1971) and Hirt and Cook (1972) for application of free surface flows.

The MAC method uses a layer of imaginary cells around the boundary of the physical domain necessitating the updating of the boundary conditions after every change in internal velocity and pressure values. The MAC method has been extensively used by many researchers to solve for the flow field in complex geometries. For example, Braza, Chassaing and Ha-Minh (1986) have obtained the unsteady wake behind a circular cylinder using the MAC method. Mukhopadhyay, Biswas and Sundararajan (1993) have obtained the periodic wake behind a rectangular obstacle. In fact, MAC method has been successfully used even to simulate highly unsteady turbulent flows (Robichaux, Tafti and Vanka, 1992). It has been experienced that the MAC method is indeed very efficient in study of temporal flow development but it has stability restrictions on the time increment, which slows down the calculation for steady flow considerably.

Since implicit methods have no such restrictions, they are more attractive. Patankar and Spalding (1972) have introduced an efficient method know as SIMPLE (Semi-Implicit Method for Pressure Linked Equations). This method is based on a finite-volume discretization of the governing equations on a staggered grid. In order to improve the convergence involved in the pressure-velocity coupling, several variants of SIMPLE algorithm have been developed. The SIMPLER algorithm of Patankar (1981) and the SIMPLEC algorithm of Van Doormaal and Raithby (1984) are improvements on SIMPLE. Although the changes to incorporate SIMPLEC into SIMPLE algorithm are minor, the consequences can be great as it eliminates the approximations made in SIMPLE while deriving the pressure-velocity

corrections. A comparative illustration of the operator splitting algorithm, viz., the PISO of Issa (1986) and the SIMPLE family of algorithms have been reported by Jang, Jetli and Acharya (1986).

Garg and Maji (1987) have applied SIMPLEC (Van Doormaal and Raithby, 1984) method for solution of viscous flows through periodically converging –diverging tubes. In another numerical investigation, Velusamy and Garg (1993) have solved the complete set of Navier-Stokes equations for three-dimensional developing flow in elliptic cross-section ducts. Application of finite volume methods using non-orthogonal coordinates and collocated grids is reported by Rhie and Chow (1983) and Peric (1985). Peric et al. (1988) have shown that collocated arrangement converges faster than the staggered variable arrangement and has advantages when extensions such as multigrid techniques and non-orthogonal grids are considered. It maybe worthwhile to note from Benard and Thompson (1984) that while staggered grid is a direct remedy to avoid pressure split with conventional finite difference interpolation of flow variables, proper interpolation of velocities still remain crucial to avoid oscillatory velocity field. An appropriate pressure interpolation avoids the pressure splits in collocated grid arrangement. A finite volume based procedure has been successfully developed using such collocated velocities and pressure. The concept of momentum interpolation of cell face pressure from nodal values has established an effective equivalence in the methods for staggered and collocated arrangements. Mukhopadhyay et al. (1993) has developed a numerical method for predicting viscous flows for incompressible

geometries. Integral mass and momentum conservation equations are deployed and these are discretized into algebraic form through numerical quadrature. The physical domain is divided into a number of non-orthogonal control volumes which are isoparametrically mapped on to standard rectangular cells. Numerical integration for unsteady momentum equation is performed over such non-orthogonal cells. The algorithm is tested on some complex problems. The results exhibit good accuracy and justify the applicability of the algorithm.

Kobayashi and Pereira (1991) have modified the momentum interpolation method suggested by Peric (1995) and named it as Pressure-Weighted Interpolation Method-Corrected (PWIMC). In this method, the non-orthogonal terms in the momentum equations were solved explicitly, whereas in the pressure-corrections they were dropped.

It is clear that substantial progress has been made for the development of algorithms for complex incompressible flow simulations but none of the prescriptions is universal. Depending on the nature of flow and geometry etc., one can always go for the best-suited discretization procedure (see Vanka, 1987; Fletcher, 1988). It is very difficult to be conclusive about any algorithm with its universal sense of applicability. However the finite volume algorithm developed by Eswaran and Prakash (1998) for solving time dependent three-dimensional full Navier-Stokes equation has the following advantages:

- It uses collocated grid arrangement, hence all the advantages of collocated grid arrangement are gainfully utilized.

- The essence of the algorithm is SMAC so it is suitable for modeling unsteady flows (see Kim and Benson, 1992).

- The governing equations are discretized in the physical plane itself without coordinate transformation.

This algorithm has been used to solve the flow problem and extended to solve the energy equation for the present work.

# Chapter 3

# Mathematical Formulation

## 3.1  Introduction

Arising out of the practical importance of the flow configuration and thermal conditions as described in the previous chapter, we a need is felt to compute three-dimensional flow in a horizontal channel with a built-in circular tube. This numerical simulation is capable of providing with quantitative information of flow structure and temperature distribution in the entire domain with their dependence on various governing parameters.

## 3.2  Statement of the Problem

The computational domain is shown in Figure 3.1. Two flat plate fins form a channel of height H, width B = 11.25H and length L = 25H. The circular tube of diameter D = 5H is located at a distance $L_1$= 1.25D from the inlet. The blockage ratio, D/B is kept fixed to 0.44.

The flow field around the circular tube in a channel is characterized by the following parameters (Figure 3.1):

- The Reynolds number.
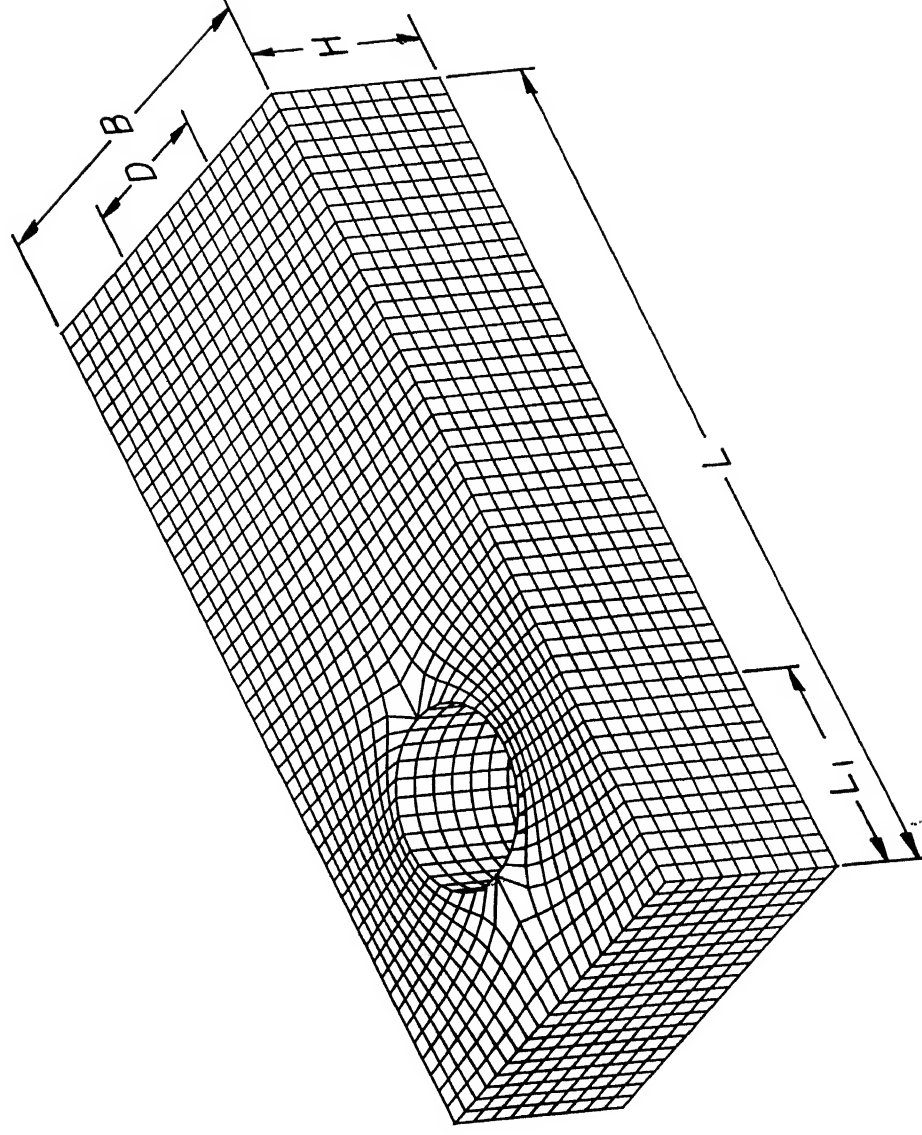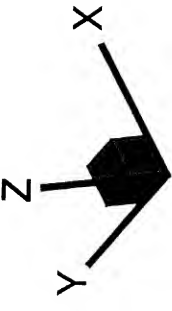
The grid-system and the computational domain
Figure 3.1

- The inverse blockage ratio D/B
- The position of the cylinder in the channel (L1/L)
- The velocity profile at the channel inlet
- The relative channel height (H/B)

These parameters determine the structure of the vortical motion in the wake.

## 3.3 Governing Equations

The three-dimensional Navier-Stokes equations for laminar flow of an arbitrary spatial control volume V bounded by a closed surface S can be expressed in the following general convection-diffusion-source integral form:

$$\frac{\partial}{\partial t}\int_V \rho \, dV \;+\; \int_S \rho\, u \cdot dS \;=\; 0 \tag{3.1}$$

$$\frac{\partial}{\partial t}\int_V \rho \phi \, dV \;+\; \int_S \left[\rho\, u \phi - \Gamma_\phi \nabla\phi\right]\cdot dS \;=\; \int_V S_\phi dV \tag{3.2}$$

Where $\rho$ represents the fluid density, $u$ is the fluid velocity, $\phi$ stands for any vector component or scalar quantity, $S_\phi$ is the volumetric source term. For incompressible flow of Newtonian fluid, the equation takes the form

$$\int_{S} u.dS = 0 \tag{3.3}$$

$$\frac{\partial}{\partial t} \int_{V} \rho \phi \, dV \quad + \quad \int_{S} [\rho u \phi - \Gamma_{\phi} \nabla \phi].dS = \int_{V} S_{\phi} dV \tag{3.4}$$

and the source term for momentum equation becomes $-\frac{1}{\rho} \int_{S} p \, I.dS$ where $\mathbf{I}$ is the unit tensor.

In this formulation we work with **Cartesian components** of velocity. So $\phi$ can be the three-cartesian components of velocity u, v, w as well as any scalar e.g., temperature which need to be determined. It is to be noted that **equation 3.2 is a perfectly general equation** from which the three fundamental equations of fluid mechanics (i.e., Continuity, Momentum and Energy) can be derived.

**Table 3.1 :** Values of the variables in the general transport equation 3.2.

| Equation | $\phi$ | $\Gamma_{\phi}$ | $S_{\phi}$ |
|----------|--------|-----------------|------------|
| Continuity | 1 | 0 | 0 |
| Momentum | $u_j$ | $\mu$ | $-\dfrac{\partial p}{\partial x_j}$ |
| Energy | T | $k/c_P$ | 0 |

# 3.4 The Grid

Figure 3.1 shows the three-dimensional grid used for our present computation. The grid generation techniques and its properties are described in brief in the following sections.

## 3.4.1    Grid Generation Technique

A differential equation method has been used for the generation of the three-dimensional grid. The initial grid is generated by the method of transfinite interpolation. This method essentially uses linear interpolation scheme to compute the interior points by using the coordinate values from the boundaries. The algebraic grid so generated in general is not smooth. This is because of the fact that the slope discontinuities at the boundary propagate in the interior of the domain. So the mesh obtained by algebraic mapping is further improved by the use of Partial Differential Equations (PDE). In this technique, a system of PDEs is solved for obtaining the location of the grid points in the physical space, whereas in the computational space is of rectangular shape with uniform spacing.

All the three types of partial differential equations, namely elliptic, parabolic and hyperbolic are used for grid generation. Elliptic equations are common for closed geometries. Hyperbolic equations are used for domains where outer boundary is not prescribed. Use of parabolic equations provides the advantage of both, speed (marching nature, hyperbolic) and smoothness

(diffusive nature, elliptic). Parabolic grid generators are in development stage and many issues like perfection, robustness of technique, specification of the control function, are yet to be resolved. The present grid is developed on the basis of elliptic grid generators.

Any grid generator system demands geometric information to be fetched from the boundaries. Hence the steady state boundary valued nature of elliptic equations makes them most favorite and most widely used grid generators. A Laplace equation or a Poisson equation with a Dirichlet boundary condition can be used for this purpose. Standard Poisson equation is of the form

$$\nabla^2 \xi = P$$
$$\nabla^2 \eta = Q \tag{3.5}$$

Where P and Q are known as control functions.
If $P = Q = 0$ then
The equation gets modified to Laplace form as

$$\nabla^2 \xi = 0$$
$$\nabla^2 \eta = 0 \tag{3.6}$$

The above equations can be solved by finite difference techniques to get the location of the interior points from the boundary. The initial guess needed to solve the Laplace equation can be generated using algebraic mapping.

## 3.4.2    A Note on Control Functions

The laplacian operator can provide highly smooth grids. The grid lines tend to be equally spaced in the absence of boundary curvature but they show a tendency to concentrate near the concave boundaries. This may prove as a drawback when the accumulation of grid lines is enforced in some specific region. Such a control on the grid lines can be obtained by proper selection of control functions P and Q. The other objective of the use of control functions is enforcing the orthogonality over the selected edges. Such boundary orthogonality simplifies the application of boundary conditions. The use of control functions is however associated with additional complexity in the transformed domain.

## 3.4.3    Computational Procedure for Grid Generation

The algorithm used for the generation of the present grid can be outlined as follows:

1. Take the input in the form of geometric data.

2. Define the computational grid (on $\xi$, $\eta$ plane) based on the number of grid points.

3. Define the boundary points along the edges of the physical domain.

4. Generate an initial guess for the Laplacian by algebraic grid generation method. In this step just a linear interpolation scheme is used to compute the interior points.

5. The guess is improved a little by adopting simple four-point formula.

6. The actual Laplacian is in the form of

$$ax_{\xi\xi} - 2bx_{\xi\eta} + cx_{\eta\eta} = 0$$
$$ay_{\xi\xi} - 2by_{\xi\eta} + cy_{\eta\eta} = 0$$

(3.7)

where

$$a = x_\eta^2 + y_\eta^2$$

$$b = x_\xi x_\eta + y_\xi y_\eta$$

$$c = x_\xi^2 + y_\xi^2$$

is solved till convergence is obtained to get the final grid.

## 3.4.4 Grid Property Evaluation

Truncation error of numerical solutions depends upon the grid on which the discretized approximation of the differential equation is solved. A desirable grid should have minimum truncation error. Certain properties of the grid are found to have strong effect on the truncation error. Parameters that effect these properties can be used to express the quality of the grid. The parameters are

- Transformation Jacobian.

- Skewness.

- Aspect ratio.

- Adjacent cell ratio.

## 1.Transformation Jacobian

The transformation Jacobian represents the local area-scaling factor for the grid generated. The determinant of the Jacobian matrix should not become zero if the mapping is to remain one to one. The quantity $|J| = 0$ will lead to a situation of an elemental area (or volume) in the transformed domain being mapped onto a point in the physical domain. Such a mapping is not acceptable.

## 2. Skewness

Skewness is a measure of non-orthogonality between two intersecting grid lines. Higher the skewness, higher will be the truncation error due to loss of independence between the grid lines. Many methods are available to evaluate the cell skewness. These methods are stated in the following section

- Intersection Angle

The intersection angle, $\theta$ between two grid lines is calculated. It is desirable that the intersection angle be 90°, however, this is not always possible. At

least, it is desirable to maintain the intersection angle in the range of $45° \leq \theta \leq 135°$ (Figure 3.2)

- Length of diagonals

In this method the skewness is calculated by using the length for the diagonals of a grid cell. For the grid cell ABCD as shown in Figure 3.3, the skewness is calculated as

$$\text{Skewness} = 1 - \frac{\text{Length of smaller diagonal}}{\text{Length of larger diagonal}} = 1 - \frac{BD}{AC}$$

- Area of triangles formed by the diagonals

In this method, skewness is calculated using the area of the triangles formed by the diagonals and the four sides of a grid cell.

$$\text{Skewness} = \frac{\text{Area of the smallest triangle}}{\text{Area of the biggest triangle}} = \frac{\triangle ODC}{\triangle OAB}$$

In the above two methods, normally the maximum allowable limit for skewness is taken around 0.5.

- Aspect Ratio

This is the maximum ratio between any of the two adjacent sides of a cell. Aspect ratio of less than 6 is desirable. It should not exceed 20.
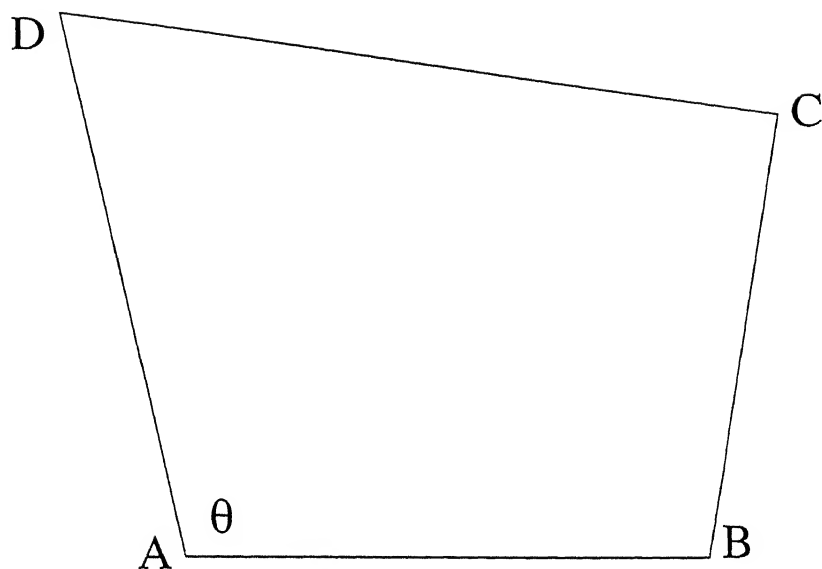
Skewness calculation based on the intersection angle.

Figure 3.2
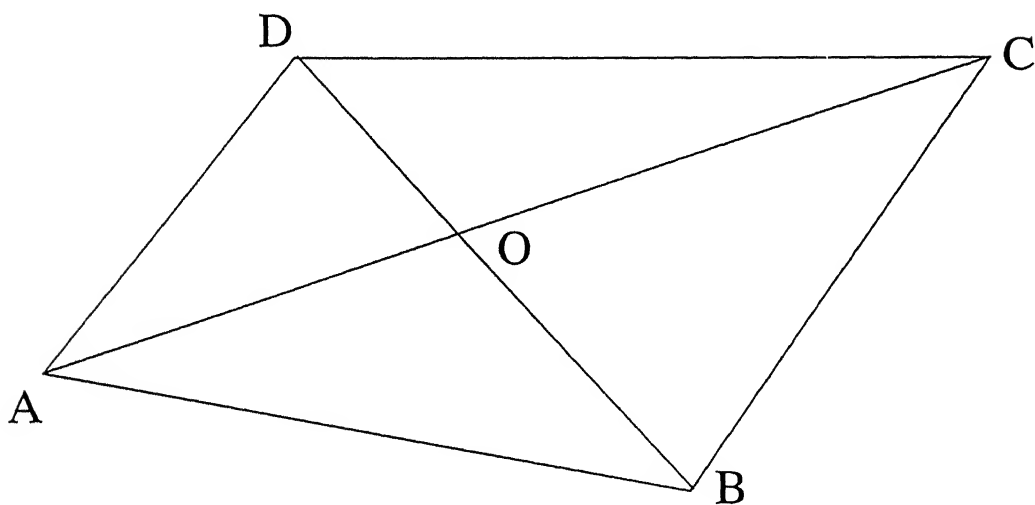


Skewness calculation based on the length of the diagonal.

Figure 3.3

- Adjacent Cell Ratio

This is the measure of grid smoothness. It is the ratio of the areas of two adjacent cells. It is desirable to have it close to one.

## 3.5 Boundary Conditions

The governing differential equations are elliptic in space and parabolic in time. We need the boundary conditions for all the confining surfaces. The boundary conditions of interest in the present investigation are

- Top and bottom plates

$$u = v = w = 0 \qquad \text{(No Slip boundary condition)}$$

$$\frac{\partial p}{\partial z} = 0$$

$$T = T_w \qquad (T_w \text{ represents wall temperature})$$

- Side Wall

$$\frac{\partial u}{\partial y} = \frac{\partial w}{\partial y} = 0, \quad v = 0 \quad \text{(Free Slip boundary condition)}$$

$$\frac{\partial p}{\partial y} = 0$$

$$\frac{\partial T}{\partial y} = 0$$

- Channel Inlet

$$u = u_\infty, \quad v = w = 0$$

$$\frac{\partial p}{\partial x} = 0$$

$$T = T_\infty$$

- Channel Exit

There is no unique prescription for outflow conditions. The evolution of mass flux through open boundaries with time is found by means of a discrete radiation condition (Orlanski 1976), which allows changes inside the flow field to be transmitted outward, but not vice-versa. Thus, a disturbance (such as a moving eddy) created inside the computational domain can leave the domain through an open boundary, but it cannot reenter. The discrete radiation condition allows the calculations to be made with fewer grid cells (i.e., less storage and computer time) than might otherwise be necessary with fixed flux condition. Orlanski condition is expressed as follows:

$$\frac{\partial \phi}{\partial t} + U_{av.} \frac{\partial \phi}{\partial x} = 0 \quad \text{(where } \phi \text{ represents u, v, w or T)}$$

$$p = p_{\infty}$$

- Obstacle

$$u = v = w = 0$$

$$\frac{\partial p}{\partial n} = 0 \qquad \text{(where n signifies normal direction)}$$

$$T = T_w$$

# Chapter 4

# Discretization Procedure and Solution Algorithm

## 4.1 Introduction

In order to solve numerically the governing equations in the prescribed computational domain with given initial and boundary conditions, two major discretization steps have to be performed. First the domain must be discretized, resulting in the numerical grid used for the computation. An explanation about the grid generation procedure was given in Chapter-3. The governing equations are discretized on the basis of this numerical grid. Various ways of discretization can be applied to the above set of partial differential equations. The most common methods are those using finite differences, finite volumes and finite elements. In the present work, a finite volume scheme was chosen for the spatial discretization of the governing equations. Thereby, a conservative formulation of the discretization was possible, assuring automatically the satisfaction of the global balance of the conserved quantities, independently of the coarseness of the numerical grid.

# 4.2 Finite-volume Method

The conservation equations are discretized employing the finite-volume approach of Eswaran and Prakash (1998). The solution domain is divided into a number of contiguous (finite) control volumes (CV). The control volumes are defined by the coordinates of their vertices, which are assumed to be connected by straight lines. The coordinates of the control volume vertices are calculated by the grid generation procedure. A **collocated grid** arrangement is employed and all the dependent variables (u, v, w, p, T) are defined at the same location, the centroid of the control volume (Figure 4.1). E, W, N, S, T and B indicate the six neighboring control volume centers for the east, west, north, south, top and bottom neighbors. The face center points e, w, n, s, t and b are located at the intersection of the lines joining the midpoints of the opposite edges. For example, te, be, ne and se are the midpoints of the edges that form the east face with e as the center of the cell face.

The collocated grids have the following advantages over the staggered grids, especially when the non-orthogonal coordinates are used:

- All variables share the same location; hence, there is only one set of control volume.
- The convection contribution to the coefficients in the discretized equations is same for all variables.

- For complex geometries Cartesian velocity components can be used in conjunction with non-orthogonal coordinates, yielding simpler equations than when coordinate oriented velocity components are employed.
- There are fewer constraints on the numerical grid, since there is no need to evaluate the grid sensitive curvature terms.

Before the time stepping can be done it is necessary to calculate geometrical parameters. These parameters include the surface vectors for the six faces e, w, n, s, t, b for each finite volume and its volume.

## 4.3 Surface areas and Volumes

The finite volume vertices are numbered 1 to 8 in the manner shown in Figure 4.1. The outward surface normals and volume can be found in the following manner as suggested by Kordulla and Vinokur (1983) and Eswaran et al.(1995)

Defining $\mathbf{r}_{ij} = \mathbf{r}_i - \mathbf{r}_j$ where $\mathbf{r}_i$ and $\mathbf{r}_j$ are the position vectors of points i and j respectively, we have for

- East Face

$$\mathbf{S}_e = \frac{1}{2}\left(\mathbf{r}_{74} \times \mathbf{r}_{83}\right) \qquad (4.1)$$
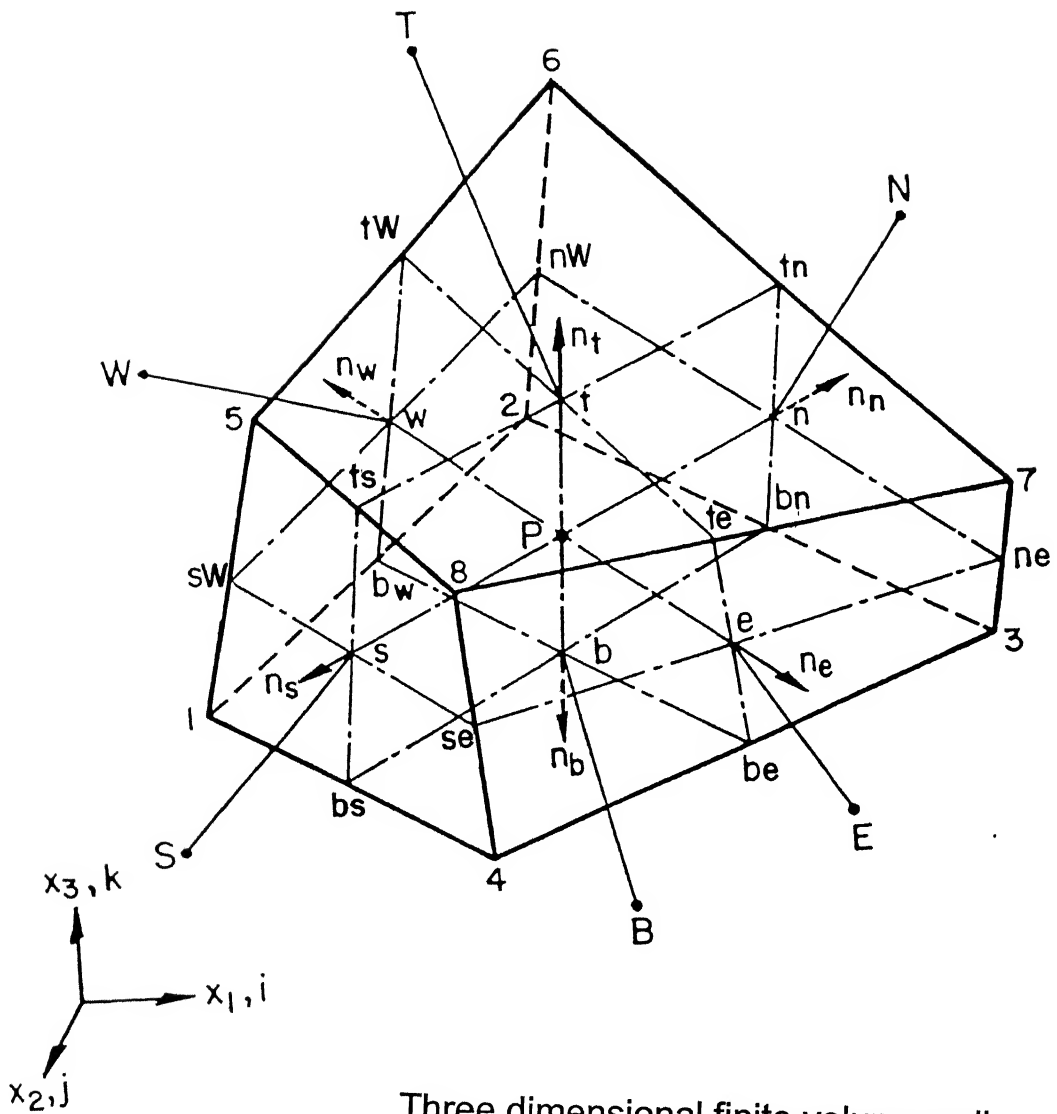
Three dimensional finite volume cell
Figure 4.1

West Face

$$S_w = \frac{1}{2}\left(r_{16} \times r_{52}\right)$$
(4.2)

- North Face

$$S_n = \frac{1}{2}\left(r_{27} \times r_{63}\right)$$
(4.3)

- South Face

$$S_s = \frac{1}{2}\left(r_{18} \times r_{45}\right)$$
(4.4)

- Top Face

$$S_t = \frac{1}{2}\left(r_{75} \times r_{68}\right)$$
(4.5)

- Bottom Face

$$S_b = \frac{1}{2}\left(r_{13} \times r_{24}\right)$$
(4.6)

The volume of the cell is calculated from the cell coordinates, with the assumption that the linear segments to form the six cell faces join the cell corners (Eswaran, 1995).

$$V = \frac{1}{3} \overrightarrow{r_{71}} \cdot (\overrightarrow{S}_s + \overrightarrow{S}_b + \overrightarrow{S}_w) \tag{4.7}$$

## 4.4 Discretization Procedure

The main steps of the discretization procedure to calculate the convection and the diffusion fluxes and source terms are outlined below. The rates of change and source terms are integrated over the cell volume, whereas the convection and the diffusion terms form the sum of fluxes through the faces of the control volume.

## 4.4.1 Discretization of the Continuity Equation

Equation 3.1 is discretized in the following way:

$$\int_S \rho u \cdot dS \approx \sum_{j=e,w,n,s,t,b} \rho (u \cdot S)_j = \sum_j \rho u_j \cdot S_j \tag{4.8}$$

where $S_j$ is the surface vector representing the area of the $j^{th}$ cell face and $u_j$ is the velocity defined at the face center j.

The discretized form the continuity equation is as the following:

$$\sum_j F_j = F_e + F_w + F_n + F_s + F_t + F_b = 0 \tag{4.9}$$

where the $F_j$ is the outward mass-flux through face j, defined by:

$$F_j = \rho u_j \cdot S_j$$

# 4.4.2. Discretization of the General Equation

## (a) Rate of Change

The value of the dependent variable $\phi$ at the centroid of the control volume (the geometric center) represents an average over the CV as a whole. Thus

$$\frac{\partial}{\partial t} \int_V \rho\phi \, dV \approx \frac{(\rho\phi V)_P^{n+1} - (\rho\phi V)_P^{n}}{\Delta t} \approx \rho V \frac{\phi_P^{n+1} - \phi_P^{n}}{\Delta t} \quad (4.10)$$

where V is the volume of the cell.

## (b) Convection Fluxes

The surface integral over convection flux of variable $\phi$ can be approximated in the following form

$$\int_S \rho u\phi \cdot dS \approx \sum_j \rho\phi_j(u \cdot S)_j = \sum_j F_j\phi_j \quad (4.11)$$

where $\phi_j$ is the value of $\phi$ at the center of face j. Thus

$$\int_S \rho u \phi \cdot dS \approx F_e \phi_e + F_w \phi_w + F_n \phi_n + F_s \phi_s + F_t \phi_t + F_b \phi_b \qquad (4.12)$$

where, $\phi_e$ is the (interpolated) value of the variable $\phi$ at the east face center, etc. This can be evaluated by using a central difference linear interpolation etween the neighboring nodal values $\phi_P$ and $\phi_E$. At east face the value of $\phi_e$ is given by

$$\phi_e = \frac{V_E}{V_E + V_P} \phi_P + \frac{V_P}{V_E + V_P} \phi_E \qquad (4.13)$$

where $V_E$ and $V_P$ are volumes of the cells around the points E and P respectively and $\phi_E$ and $\phi_P$ are the values of the dependent variables at these points. In a collocated grid system, all dependent variables are defined at the same location hence exactly the same interpolation scheme is used to express all of them at the interfaces. The central difference approximation to compute the convection may lead to numerical stability problems. Therefore the convection flux is blended with a first-order upwind differencing scheme (UDS), and the difference between the central difference scheme (CDS) and UDS approximations as

$$F_e \phi_e = \left(F_e \phi_e\right)^{UDS} + \gamma [\left(F_e \phi_e\right)^{CDS} - \left(F_e \phi_e\right)^{UDS}] \qquad (4.14)$$

The upwind differencing scheme is based on the assumption that the convected cell face value is equal to that at the upstream cell along the same

coordinate direction. Thus, the value $\phi_e$ at the east face is assigned the value $\phi_P$ if $u_e \geq 0$, i.e., the flux $F_e$ is negative. This can be conveniently summarized as

$$F_e\phi_e = \phi_P[[F_e,0]] - \phi_E[[-F_e,0]] + \gamma \left\{ F_e\left( \frac{V_E}{V_E + V_P}\phi_P + \frac{V_P}{V_E + V_P}\phi_E \right) \right.$$
$$\left. - \phi_P[[F_e,0]] + \phi_E[[-F_e,0]] \right\} \qquad (4.15)$$

The symbol $[[,]]$ signifies greater of the two quantities enclosed inside the brackets. Similar expressions can be written for the other cell faces (Eswaran et al. 1995)

$$F_w\phi_w = \phi_P[[F_w,0]] - \phi_W[[-F_w,0]] + \gamma \left\{ F_w\left( \frac{V_P}{V_w + V_P}\phi_W + \frac{V_W}{V_W + V_P}\phi_P \right) \right.$$
$$\left. - \phi_P[[F_w,0]] + \phi_W[[-F_w,0]] \right\} \qquad (4.16)$$

$$F_n\phi_n = \phi_P[[F_n,0]] - \phi_N[[-F_n,0]] + \gamma \left\{ F_n\left( \frac{V_N}{V_N + V_P}\phi_P + \frac{V_P}{V_N + V_P}\phi_N \right) \right.$$
$$\left. - \phi_P[[F_n,0]] + \phi_N[[-F_n,0]] \right\} \qquad (4.17)$$

$$F_s\phi_s = \phi_P[[F_s,0]] - \phi_S[[-F_s,0]] + \gamma \left\{ F_s \left( \frac{V_P}{V_S + V_P}\phi_S + \frac{V_S}{V_S + V_P}\phi_P \right) \right.$$
$$\left. -\phi_P[[F_s,0]] + \phi_S[[-F_s,0]] \right\} \qquad (4.18)$$

$$F_t\phi_t = \phi_P[[F_t,0]] - \phi_T[[-F_t,0]] + \gamma \left\{ F_t \left( \frac{V_T}{V_T + V_P}\phi_P + \frac{V_P}{V_T + V_P}\phi_T \right) \right.$$
$$\left. -\phi_P[[F_t,0]] + \phi_T[[-F_t,0]] \right\} \qquad (4.19)$$

$$F_b\phi_b = \phi_P[[F_b,0]] - \phi_B[[-F_b,0]] + \gamma \left\{ F_b \left( \frac{V_P}{V_B + V_P}\phi_B + \frac{V_B}{V_B + V_P}\phi_P \right) \right.$$
$$\left. -\phi_P[[F_b,0]] + \phi_B[[-F_b,0]] \right\} \qquad (4.20)$$

In a fully implicit method the upwind parts of the above equations are implicit and they are incorporated in the coefficients of the unknown velocity during the pressure-velocity iterations. The CDS terms on the other hand are evaluated using the previous iteration values and used as a source term on the right side of the same equation. This is the so-called deferred correction approach of Khosla and Rubin (1974). Multiplication of the explicit part by a factor of $\gamma$ ($0 \leq \gamma \leq 1$) allows the introduction of numerical diffusion. For the first order upwind difference scheme, $\gamma = 0$ and for the second order central difference, $\gamma = 1$. The deferred correction approach enhances the diagonal dominance of the coefficient matrix. However, the

present solution scheme being explicit, the formal accuracy depends on the value of $\gamma$.

## (c) Diffusion Fluxes

Historically Peric (1985) developed the expression for the diffusion fluxes for the finite volume approach for the first time. However, the exact expressions in three dimensions are not explicitly available in open literature. Eswaran and Prakash (1998) have explained the philosophy of defining the diffusion fluxes at the cell interfaces in a lucid manner. Eswaran and Prakash (1998) evaluate the diffusion flux of a variable $\phi$ through the cell faces in the following manner

$$\int_S \Gamma_\phi \nabla \phi \cdot \mathbf{dS} \approx \sum_{j=e,w,n,s,t,b} \left( \Gamma_\phi \nabla \phi \cdot \mathbf{S} \right)_j = \sum_j - F_j^d \qquad (4.21)$$

For any face we can write

$$S_j = \alpha_1 n^1 + \alpha_2 n^2 + \alpha_3 n^3 \qquad (4.22)$$

where $n^1$, $n^2$ and $n^3$ are any three linearly independent (not necessarily orthogonal) unit vectors. Therefore

$$\nabla \phi \cdot S_j = \nabla \phi \cdot \left( \alpha_1 n^1 + \alpha_2 n^2 + \alpha_3 n^3 \right) \qquad (4.23)$$

$$= \alpha_1 \nabla\phi \cdot n^1 + \alpha_2 \nabla\phi \cdot n^2 + \alpha_3 \nabla\phi \cdot n^3$$

If $\Delta\phi^1$, $\Delta\phi^2$, $\Delta\phi^3$ are the differences in $\phi$ between the two ends of the line segments $\Delta x^1$, $\Delta x^2$, $\Delta x^3$, then

$$\Delta\phi^1 = \nabla\phi \cdot \Delta \mathbf{x}^1, \qquad \Delta\phi^2 = \nabla\phi \cdot \Delta \mathbf{x}^2, \qquad \Delta\phi^3 = \nabla\phi \cdot \Delta \mathbf{x}^3 \qquad (4.24)$$

If $\Delta x^1$, $\Delta x^2$, $\Delta x^3$ are in the directions of $n^1$, $n^2$ and $n^3$ respectively, then it follows from equation (4.24) that

$$\frac{\Delta\phi^1}{\Delta x^1} = \nabla\phi \cdot n^1, \quad \frac{\Delta\phi^2}{\Delta x^2} = \nabla\phi \cdot n^2, \quad \frac{\Delta\phi^3}{\Delta x^3} = \nabla\phi \cdot n^3 \qquad (4.25)$$

where $\Delta x^1$, $\Delta x^2$ and $\Delta x^3$ are the magnitudes of $\Delta \mathbf{x}^1$, $\Delta \mathbf{x}^2$ and $\Delta \mathbf{x}^3$. Combining equations (4.23) and (4.25) we have

$$\nabla\phi \cdot \mathbf{S} = \alpha_1 \frac{\Delta\phi^1}{\Delta x^1} + \alpha_2 \frac{\Delta\phi^2}{\Delta x^2} + \alpha_3 \frac{\Delta\phi^3}{\Delta x^3} \qquad (4.26)$$

To obtain $\alpha_1$, $\alpha_2$ and $\alpha_3$, we express

$$\mathbf{n}^1 = \begin{pmatrix} n_{11} & n_{12} & n_{13} \end{pmatrix}$$
$$\mathbf{n}^2 = \begin{pmatrix} n_{21} & n_{22} & n_{23} \end{pmatrix} \qquad (4.27)$$
$$\mathbf{n}^3 = \begin{pmatrix} n_{31} & n_{32} & n_{33} \end{pmatrix}$$

where $n_{11}$, $n_{12}$, $n_{13}$ are the Cartesian components of $\mathbf{n}$ and which can be

easily determined by $\dfrac{\Delta \mathbf{x}_1^1}{\Delta \mathbf{x}^1}$, $\dfrac{\Delta \mathbf{x}_2^1}{\Delta \mathbf{x}^2}$, $\dfrac{\Delta \mathbf{x}_3^1}{\Delta \mathbf{x}^3}$, where $\Delta \mathbf{x}_1^1$, $\Delta \mathbf{x}_2^1$, $\Delta \mathbf{x}_3^1$ are the

three components of vector $\Delta \mathbf{x}^1$, etc. The other values $n_{21} \ldots n_{33}$ can be

similarly obtained. Hence equation (4.22) can be written as

$$\begin{bmatrix} n_{11} & n_{12} & n_{13} \\ n_{21} & n_{22} & n_{23} \\ n_{31} & n_{32} & n_{33} \end{bmatrix}^T \begin{bmatrix} \alpha_1 \\ \alpha_2 \\ \alpha_3 \end{bmatrix} = \begin{bmatrix} S_{1j} \\ S_{2j} \\ S_{3j} \end{bmatrix} \qquad (4.28)$$

where $S_{1j}$, $S_{2j}$, $S_{3j}$ are the Cartesian components of the **surface** vector

$S_j$

Using Cramers rule

$$\alpha_1 = \frac{D_1}{D}, \quad \alpha_2 = \frac{D_2}{D}, \quad \alpha_3 = \frac{D_3}{D} \qquad (4.29)$$

where D is the determinant of the coefficient matrix. $D_1$ is obtained by replacing the first column of D by the column with the elements $S_{1j}$, $S_{2j}$, and $S_{3j}$. Thus $\alpha_1$, $\alpha_2$, and $\alpha_3$ are determined.
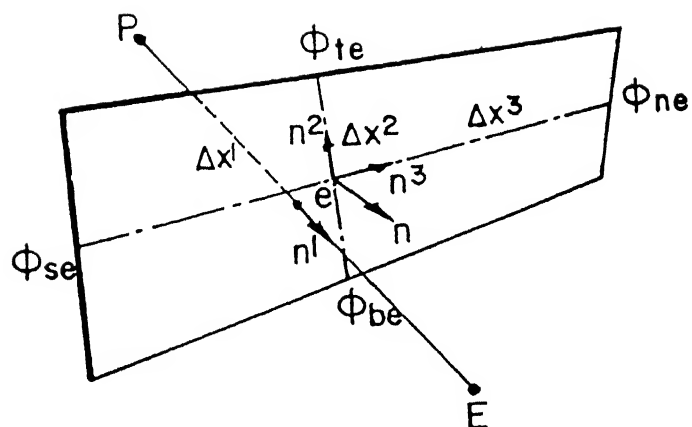
The diffusion flux is made of two distinct parts: normal derivative diffusion flux and cross derivative diffusion flux. The second part arises from the non-orthogonality of the grid. The normal derivative diffusion flux of $\phi$ through any cell face involves the values of $\phi$ at cell centers whereas the cross-derivative diffusion flux takes into account the edge center values of $\phi$. The normal derivative diffusion flux is treated implicitly and is coupled with the implicit part of the convective flux to calculate the main coefficients of the discretized equations while the cross-derivative diffusion flux is treated explicitly to avoid the possibility of producing negative coefficients in an implicit treatment. This term together with explicit part of convective flux is added to the source term. The example of the east face is taken to illustrate the diffusion model (Figure-4.2). Given the edge center values $\phi_{te}$, $\phi_{be}$, $\phi_{se}$, $\phi_{ne}$ we can get the normal diffusion term $\dfrac{\phi_E - \phi_P}{\Delta x^1}$, and the cross diffusion term $\dfrac{\phi_{te} - \phi_{be}}{\Delta x^2}$ and $\dfrac{\phi_{se} - \phi_{ne}}{\Delta x^3}$. Finally, the diffusion flux is computed by

$$F_j^d = -\Gamma_\phi \left( \alpha_1 \frac{\phi_E - \phi_P}{\Delta x^1} + \alpha_2 \frac{\phi_{te} - \phi_{be}}{\Delta x^2} + \alpha_3 \frac{\phi_{ne} - \phi_{se}}{\Delta x^3} \right) \qquad (4.30)$$

Face representation to illustrate the diffusion model
Figure 4.2

In order to calculate the edge center values for the calculation of cross-derivative diffusion flux, the following interpolation scheme is proposed:

$$\phi_{te} = \frac{V_{TE}}{V_{tot}}\phi_P + \frac{V_P}{V_{tot}}\phi_{TE} + \frac{V_T}{V_{tot}}\phi_E + \frac{V_E}{V_{tot}}\phi_T \qquad (4.31)$$

$$V_{tot} = V_{TE} + V_P + V_T + V_E$$

$$\phi_{be} = \frac{V_{BE}}{V_{tot}}\phi_P + \frac{V_P}{V_{tot}}\phi_{BE} + \frac{V_B}{V_{tot}}\phi_E + \frac{V_E}{V_{tot}}\phi_B \qquad (4.32)$$

$$V_{tot} = V_{BE} + V_P + V_B + V_E$$

$$\phi_{ne} = \frac{V_{NE}}{V_{tot}}\phi_P + \frac{V_P}{V_{tot}}\phi_{NE} + \frac{V_N}{V_{tot}}\phi_E + \frac{V_E}{V_{tot}}\phi_N \qquad (4.33)$$

$$V_{tot} = V_{NE} + V_P + V_N + V_E$$

$$\phi_{se} = \frac{V_{SE}}{V_{tot}}\phi_P + \frac{V_P}{V_{tot}}\phi_{SE} + \frac{V_S}{V_{tot}}\phi_E + \frac{V_E}{V_{tot}}\phi_S \qquad (4.34)$$

$$V_{tot} = V_{SE} + V_P + V_S + V_E$$

where, $V_{TE}$ is the volume of the cell that is located at the top-east of the cell P. The other edge center values of the dependent variables can be interpolated in a similar way.

# (d) Sources

The source term is to be integrated over the cell volume. The contribution of a source term in the discretized equation may be thought of

$$\int_V S_\phi dV \approx \left(S_\phi\right)_P V \tag{4.35}$$

Apart from the real source $S_\phi$, explicitly treated parts of the convection and diffusion fluxes maybe added to $S_\phi$. The momentum equations contain pressure terms. These terms are also treated explicitly. Its discretization is analogous to that of the ordinary diffusion flux, i.e., for the $i^{th}$ momentum equation the pressure term is

$$-\int_S p\mathbf{n}_i \cdot S \approx \sum_j p_j S_{ij} \tag{4.36}$$

where $p_j$ is the pressure at the $j^{th}$ face center and $S_{ij}$ is the $i^{th}$ component of the surface vector for face j.

# 4.5 Pressure-Velocity Coupling

To obtain the velocity and pressure field satisfying the mass and momentum conservation laws, a procedure akin to Simplified Marker and Cell (SMAC) method is used. This method offers an efficient and an easy way of pressure-

velocity coupling. It is basically a semi-explicit method. The momentum equations are discretized in an explicit manner with the exception of the pressure gradient terms that are treated implicitly, and the continuity equations are also enforced implicitly. This can be expressed mathematically by the following two discretized equations of momentum and continuity:

$$\rho V \frac{u_P^{n+1} - u_P^n}{\Delta t} + \sum_j \left( F^c + F^d \right)^n = - \sum_j p_j^{n+1} S_{ij} \qquad (4.37)$$

and

$$\sum_j F_j^{n+1} = 0 \qquad (4.38)$$

The momentum equations are solved using the guess values of velocity and pressure field. The provisional velocity components $u_i^*$ are calculated from the following equation

$$\mathbf{u}_P^* = \mathbf{u}_P^\circ - \frac{\Delta t}{\rho V_P} \left( F_P^c + F_P^d \right) + \frac{\Delta t}{\rho V_P} S_u \qquad (4.39)$$

where $\mathbf{u}_P^\circ$ is the value of velocity at earlier iteration and $S_u$ is the pressure term. This provisional velocity in general will not satisfy the continuity equation. The continuity equation (4.38) in another form reads as follows:

$$\sum_j \left( F_j^* + F_j' \right) = 0$$

$$\sum_j F_j' = -\sum_J F_j^* \qquad (4.40)$$

where $F_j^*$ is the uncorrected mass flux obtained from the provisional velocities and $F_j'$ is the mass flux correction. To evaluate the terms on the right side of equation (4.40), it is necessary that the variables (velocities and pressure) are to be known at the cell faces. Due to the non-staggered arrangement, if the variables at the cell faces are evaluated by linear interpolation between the adjacent cell center quantities then the pressure iteration does not converge. The solution leads to a *Checker Board* pressure field (i.e., spurious oscillation of pressure may occur), as shown by Rhie (1981). This problem can be circumvented by using the concept of *Momentum Interpolation* (Majumdar, 1988). The essence of the concept is that the velocities at the cell faces are computed by linear interpolation of the convective and diffusive terms but not the pressure term. Thus the method with the collocated variable arrangement relies indirectly on the staggering idea. Following this idea the interpolated velocity at the east face of the control volume given by is obtained in the following manner

$$\mathbf{u}_e = \overline{(\mathbf{v}_P, \mathbf{v}_E)} - \frac{\Delta t}{\rho} \nabla p \tag{4.41}$$

where

$$\mathbf{v}_P = \mathbf{u}_P^\circ - \frac{\Delta t}{\rho V_P}\left(F_P^c + F_P^d\right) \tag{4.42}$$

$$\mathbf{v}_E = \mathbf{u}_E^\circ - \frac{\Delta t}{\rho V_E}\left(F_E^c + F_E^d\right) \tag{4.43}$$

and the overbar indicates a linear interpolation using equation (4.13). So the uncorrected mass flux for the east face using equation (4.41) becomes

$$F_e^* = \rho\,\mathbf{u}_e \cdot \mathbf{S}_e = \rho\,\overline{(\mathbf{v}_P, \mathbf{v}_E)} \cdot \mathbf{S}_e - \Delta t \nabla p \cdot \mathbf{S}_e \tag{4.44}$$

Equation (4.44) in its generalized form for any cell face is in the form

$$F_j^* = \rho\,\mathbf{v}_j \cdot \mathbf{S}_j - \Delta t \nabla p_j \cdot \mathbf{S}_j \tag{4.45}$$

To enforce mass conservation, the velocity and pressure corrections are introduced, linked by

$$\mathbf{u}_j' = -\frac{\Delta t}{\rho} \nabla p_j' \tag{4.46}$$

This step simulates the effect of a staggered grid (face-center velocity and cell-center pressure) and reaps the benefits of faster convergence. From equation (4.46) we get the mass flux correction at the face j

$$F_j' = \rho \, u_j' \cdot S_j = -\Delta t \, \nabla p_j' \cdot S_j' \qquad (4.47)$$

Since equation (4.47) is exactly of the same form as equation for diffusion flux equation (4.21), with only the variables interchanged, therefore the same method can be used for computing $F_j'$

Combining equations (4.40), (4.45) and (4.47) yields

$$-\Delta t \, \nabla p_j' \cdot S_j = \rho \, V_j \cdot S_j - \Delta t \, \nabla p_j \cdot S_j$$

or $\qquad \Delta t \, \nabla p_j' \cdot S_j + S_m = 0 \qquad (4.48)$

$$(S_m = \rho \, V_j \cdot S_j - \Delta t \, \nabla p_j \cdot S_j)$$

which gives the *pressure correction equation*. After the solution of the pressure correction equation, the nodal velocity, mass fluxes and pressure are updated. The corrected pressure $p^{n+1}$ is obtained by

$$p^{n+1} = p^n + p' \qquad (4.49)$$

Instead of solving equation (4.37) again with the corrected pressure field, velocity calculations can be corrected in the form

$$\mathbf{u}_P' = -\frac{\Delta t}{\rho V_P} \sum_j p_j' S_{ij} \tag{4.50}$$

The corrected velocity field $u_i^{n+1}$ is then obtained by

$$u_i^{n+1} = u_i^* + u_i' \tag{4.51}$$

Using this new velocity distribution, the energy equation is discretized and solved. On integrating the conservative form of the steady state energy equation over a control volume (neglecting the dissipative terms as, it is significant for high speed flows), we arrive at the following temperature equation

$$\alpha \sum_j (\nabla T \cdot S)_j = \sum_j (\rho u_j \cdot S_j) T_j \tag{4.52}$$

which is solved iteratively to get the temperature distribution of the current time step.

The first terms of equation (4.48) and equation (4.52) are expanded following the philosophy that was followed during the discretization of

equation (4.21). Subsequent regrouping of the normal derivative terms yields the standard *Poisson Equation.* The Poisson equation can be solved by a multitude of methods. We have used the Gauss Seidel iteration method. This method is quite reliable and robust. The flow chart with the main steps of the algorithm is given in Figure 4.3.

# 4.6 Solution Algorithm

The velocity pressure and temperature fields are calculated by the following the procedure of Eswaran and Prakash (1998). The procedure can be summarized in the following way

1. Make initial guess of the pressure velocity and temperature fields. Use equations (4.41) and (4.42) to calculate cell center $\mathbf{u}_P$ and $\mathbf{v}_P$. Use linear interpolation (equation 4.12) to obtain the face center quantities $\mathbf{v}_j$.

2. Compute the mass flux through cell face j using equation (4.45) i.e.,

$$F_j^* = \rho\, \mathbf{v}_j \cdot \mathbf{S}_j - \Delta t \nabla p_j \cdot \mathbf{S}_j$$

3. Use equation (4.46) to compute the flux correction at the cell face j using equation (4.47) i.e.,
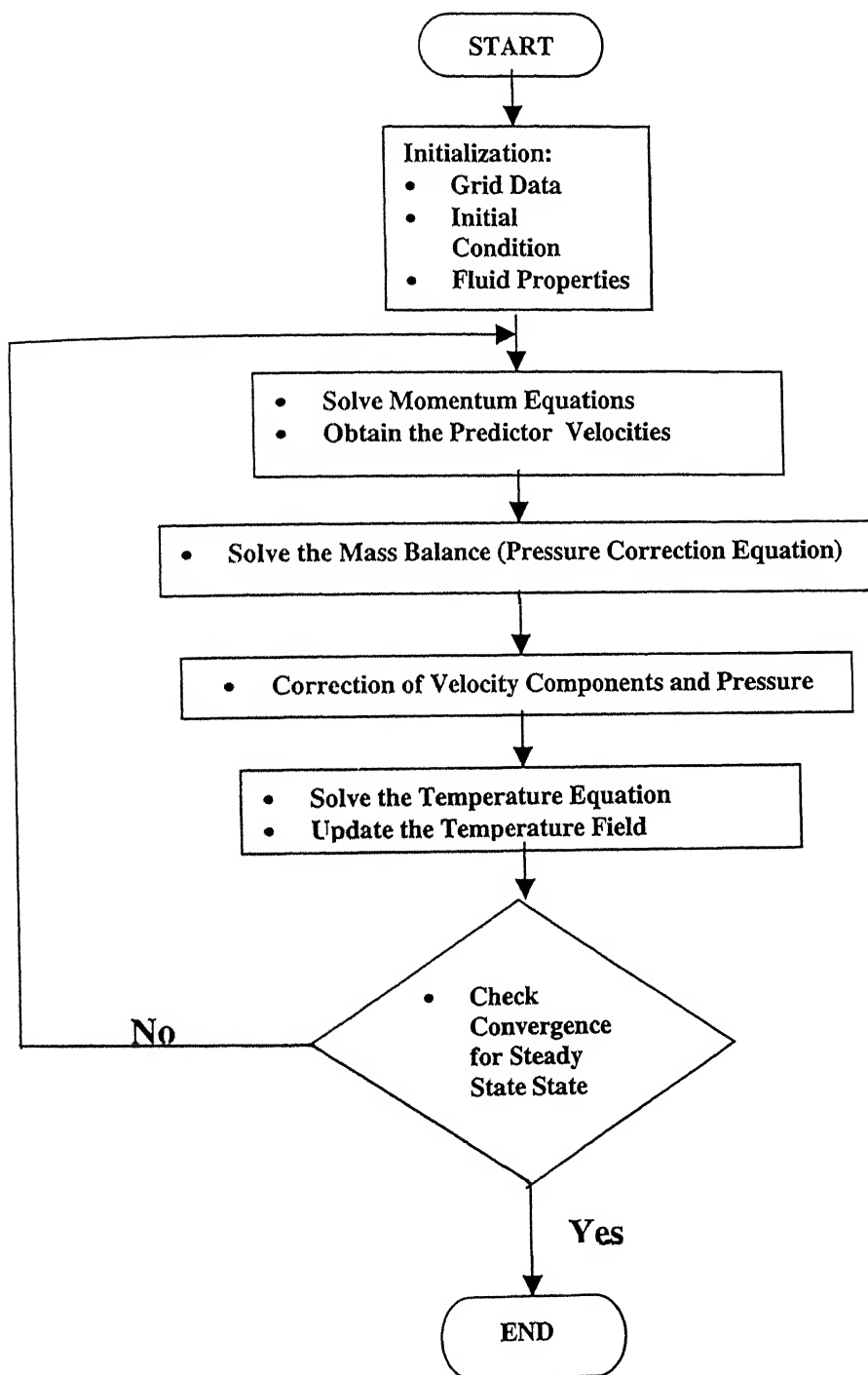
```
                        ┌─────────────┐
                        │    START    │
                        └──────┬──────┘
                               │
                               ▼
                  ┌──────────────────────────┐
                  │ Initialization:          │
                  │   • Grid Data            │
                  │   • Initial              │
                  │     Condition            │
                  │   • Fluid Properties     │
                  └────────────┬─────────────┘
                               │
   ┌───────────────────────────┤
   │                           ▼
   │        ┌──────────────────────────────────┐
   │        │  • Solve Momentum Equations      │
   │        │  • Obtain the Predictor Velocities│
   │        └────────────────┬─────────────────┘
   │                         │
   │                         ▼
   │   ┌────────────────────────────────────────────────┐
   │   │ • Solve the Mass Balance (Pressure Correction   │
   │   │   Equation)                                     │
   │   └────────────────────┬───────────────────────────┘
   │                        │
   │                        ▼
   │   ┌──────────────────────────────────────────────┐
   │   │ • Correction of Velocity Components and       │
   │   │   Pressure                                    │
   │   └────────────────────┬─────────────────────────┘
   │                        │
   │                        ▼
   │        ┌────────────────────────────────────┐
   │        │ • Solve the Temperature Equation   │
   │        │ • Update the Temperature Field     │
   │        └────────────────┬───────────────────┘
   │                         │
   │                         ▼
   │                    ◇─────────────◇
   │              No   ╱  • Check      ╲
   └─────────────────╱    Convergence   ╲
                     ╲    for Steady     ╱
                      ╲   State State   ╱
                       ◇─────────────◇
                              │
                             Yes
                              │
                              ▼
                        ┌───────────┐
                        │    END    │
                        └───────────┘
```

**Figure 4.3 Iterative Solution Scheme**

$$F'_j = -\Delta t \, \nabla p'_j \cdot S'_j$$

This is computed using the formulation for diffusion fluxes [equations (4.21 – 4.34)]. For calculating by $F'_j$, the variable $\phi$ is to be replaced by $p'$.

4. Compute the residue, $\Re$ for each cell,

$$\Re = -\sum_j F^*_j - \sum_j F'_j$$

5. Calculate the cell-center pressure correction (using Gauss-Seidel method) from the relation

$$p'_p = p'_p + \omega \frac{\Re}{a_p \, \Delta t}$$

where $\omega$ is the relaxation factor and $a_p$ stands for the diagonal coefficients of equation (4.48), which is calculated from

$$a_p = -\left[ \frac{\alpha_1}{\Delta x^1}\bigg|_w - \frac{\alpha_1}{\Delta x^1}\bigg|_e + \frac{\alpha_2}{\Delta x^2}\bigg|_n - \frac{\alpha_2}{\Delta x^2}\bigg|_s + \frac{\alpha_3}{\Delta x^3}\bigg|_s - \frac{\alpha_3}{\Delta x^3}\bigg|_t \right]$$

where $\alpha_1$, $\alpha_2$ etc. are the same as that are used in equations (4.21 – 4.34).

6. If $\Re_{rms} > \varepsilon$ go to step 3.

7. Store the updated mass flux through cell faces using equation (4.45)

$$F_j^* = \rho\, \mathbf{v}_j \cdot \mathbf{S}_j - \Delta t \nabla p_j \cdot \mathbf{S}_j$$

8. Store the updated pressure at the center of the cells

$$p_p = p_p + p_p'$$

9. Store the cell-center corrected velocity

$$\mathbf{u}_P' = -\frac{\Delta t}{\rho V_P} \sum_j p_j' S_{ij}$$

$$\mathbf{u}_P = \mathbf{u}_P + \mathbf{u}_P'$$

10. Calculate the residual for each cell

$$\widetilde{\Re} = \sum_j \left(\rho\, u_j \cdot S_j\right) T_j - \alpha \sum_j (\nabla T \cdot S)_j$$

11. Calculate the cell-center temperature using Gauss-Seidel method, to obtain

$$T_P = T_P + \Omega \frac{\widetilde{\mathfrak{R}}}{b_P \, \alpha}$$

where $\Omega$ is the relaxation factor and $b_P$ stands for the diagonal coefficients of equation (4.52) i.e., calculated from the relation

$$b_P = - a_P$$

12. If $\widetilde{\mathfrak{R}}_{rms} > \varepsilon$ go to step 10

13. Go to step 1 and repeat the process until the steady state is reached.

It can be shown that solving equation (4.40) is same as solving

$$\nabla^2 p' = - \rho \frac{\nabla \cdot u_i^*}{\Delta t}$$

and finding the corrections

$$u_i' = - \frac{\Delta t}{\rho} \nabla p'$$

such that

$$u_i^{n+1} = u_i^* + u_i'$$

$$p^{n+1} = p^n + p'$$

Thus the procedure above can be called solution of *Pressure Correction Linked Equations*.

# 4.7 Numerical Stability Considerations

Since we are using a Semi-Explicit method, which relies on explicit differences, suffer from time step restrictions. For a given mesh the choice of the time step is determined through stability analysis which has to take care two conditions. First, fluid should not be allowed to cross more than one cell in any one time step. This restriction is derived from the Courant-Friedrichs-Lewy (CFL) condition given by

$$\delta t_1 < \min\left\{ \frac{\delta x}{|u|}, \frac{\delta y}{|v|}, \frac{\delta z}{|w|} \right\} \qquad (4.52)$$

where the minimum is with respect to every cell in the domain. Typically $\delta t$ is chosen equal to one-third to two-third of the minimum cell transient time.

Secondly, when a nonzero value of kinematic viscosity is used momentum must not diffuse more than approximately one cell in one time step. A linear stability analysis shows that the restrictions on grid Fourier number will yield

$$\delta t_2 < \frac{1}{2} \frac{(\delta x)^2 (\delta y)^2 (\delta z)^2}{(\delta x)^2 + (\delta y)^2 + (\delta z)^2} \, Re \qquad (4.53)$$

Finally, the minimum of the above two time increments is chosen for computation.

# Chapter 5

# Results and Discussion

## 5.1    Introduction

A three-dimensional numerical simulation of the flow structure and the heat transfer characteristics in a rectangular channel with a built-in circular tube (Figure 1.3) are presented The geometrical configuration represents an element of a gas-liquid fin-tube crossflow heat exchanger. The following characteristic features of flow are established:

- The flow that curls around the tube separates at the downstream of the leading edge of the tube and forms the recirculation region in the tube wake with screw like motion of the helical vortex tube.

- The wake region of the tube shows strong three-dimensionality.

- The limiting streamlines on the built-in tube depict typical separation lines.

- The limiting streamlines on the bottom wall reveal presence of th saddle point of separation in front of the tube and the bottom wall junction.

- The horseshoe vortices, which form in the front of the tube near the bottom and top plates

The corresponding characteristics of heat transfer influenced by the flow structure are also established.

- The high heat transfer near the leading edge of the fins and in the region influenced by the horseshoe vortices.

- The poor heat transfer in the wake region of the tube.

For the computation of the present problem, the finite-volume method of Eswaran and Prakash (1998) is used. A $100 \times 51 \times 17$ grid-mesh is used in the present computation. The divergence-free criterion is satisfied using an upper bound of $10^{-4}$. The blockage ratio (D/B) and Reynolds number are kept fixed to 0.44 and 1000 respectively. In this work no symmetry is assumed in the midplane of the channel.

## 5.2 Flow Characteristics

In this section a detailed investigation of the flow pattern in the passage of the fin tube element (Figure 1.3) is presented. For a three-dimensional flow simulation, it becomes quite difficult to handle the enormous data and only effective use of some approaches proposed in literature can depict the flow structure. Of the possible methodologies that allow us to explore the kinematics of complex flows, the method of topological study of limiting streamlines is the most preferred one because the flow structure is best described by the topological properties inferred from computed streamlines. According to Legendre (1956), the study of the topology of three dimensional streamlines projected onto a no-slip body surface is computationally analogous to the experimental surface flow visualization. The skin-friction line field, according to the definition of Lighthill (1963),

can be regarded as the projection of the three-dimensional streamline field onto the body surface. This implies that the observed topological patterns of the limiting streamlines have significant implications for the flow evolution in the flow passage.

It becomes quite convenient to analyze the kinematic aspects of computable limiting streamlines in terms of singular points of different kinds. So it becomes important to determine these singular points from which the flow structure can be sketched. In a set of velocity vectors, by definition the singular points are those, which have zero magnitude, but their directions are indeterminate. Around a critical point, the vector field varies according to the eigenvectors and the eigenvalues of the Jacobian of the field at the detected critical point. Depending on the divergence of the shear-stress vector and the Jacobian, singular points can be classified into two main topological types. These are saddle points and nodal points. The difference between these points can be observed very clearly by seeing the corresponding portraits (Figure 5.1).

- Saddle points: - Through a saddle point only two sets of shear-stress lines pass. On each of these lines, the direction of the skin-friction vector field $\left[ \mu \dfrac{\partial u}{\partial z}, \mu \dfrac{\partial v}{\partial z} \right]$ changes sign on a surface. Depending on the type of saddle points, separation or attachment, both skin-friction directions are towards the critical point on one and both skin friction directions are away from this point on the other. In a two-dimensional flow there exists
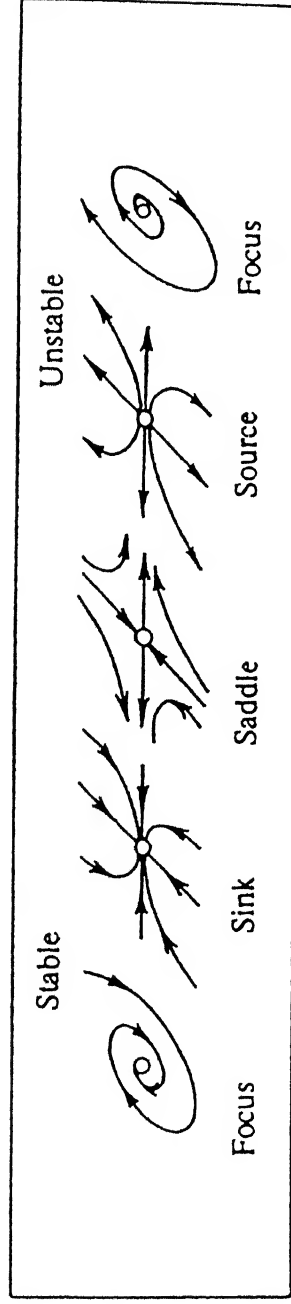
Schematic diagrams of nodal and saddle points
Figure 5.1

special streamlines, called separation lines, which conveniently divide the flow into two distinct regions. Such streamlines originate at saddle points. The counterparts to these separation lines in three-dimensional flows are special streamsurfaces. This implies that the saddle points act as barriers in the field of vectors.

- Nodal points:- These are points through which an infinite number of shear-stress lines pass. Nodal points are of two types, namely, regular nodal points (or nodes) and foci (or spiral nodes). Nodal points of attachment act as sources of skin-friction lines that emanate from the point and spread out over the surface. Nodal points of separation, on the other hand, act as sinks where the skin friction lines circumscribing the body vanish. Foci and nodes differ in the orientation of their chosen field. For a singular point defined as a spiral node, all shear-stress lines spiral onto or out of this point. Emanating from this type of node are two straight critical lines.

The motivation behind undertaking topological study of the vector field is to classify some mechanisms that may add to the heat-transfer capability of the system. A better understanding of the flow is essential.

# 5.2.1 Flow Topology on the Horizontal and the Vertical Planes of the Channel

Figure 5.2 shows the streamline plot of the time-averaged flow on the horizontal midplane of the channel at $z$=H/2. The figure clearly shows the two symmetrical standing vortices. The flow separation and the wake formation are clearly visible. The recirculation in the wake region of the tube is clearly established. Figure 5.3 illustrates the streaklines, showing the path of the fluid particles on their way through the channel commencing at various starting points on a vertical plane. The flow pattern clearly shows the existance of a screw-like helical vortex motion in the wake region of the tube. Figure 5.4 shows the contour plot for the time averaged axial velocity, $\overline{u}$, on the horizontal midplane of the channel at z=H/2. The recirculation region is located approximately at 0.39 diameters downstream away from the tube. The zero mean velocity line indicates the boundary of the recirculation zone. Figure 5.5 shows the contour plot of the transverse mean-velocity, $\overline{v}$ on the horizontal midplane of the channel. The profile is perfectly anti-Symmetric. The maximum value of transverse mean-velocity in the wake occurs at about 0.75 diameters downstream away from the tube.

Figure 5.6 shows the distribution of time averaged pressure distribution along the tube wall. The pressure coefficient
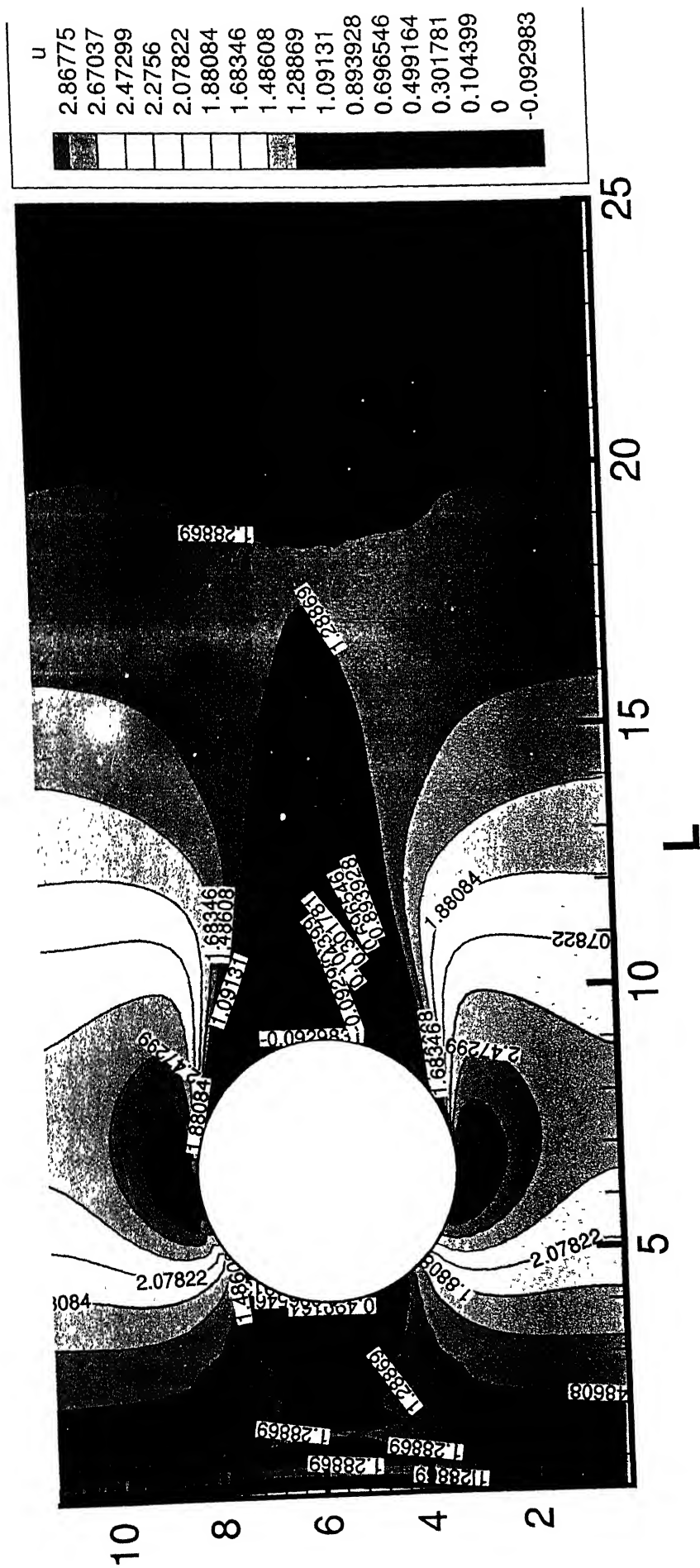
$$C_P = ( P - P_0 + \frac{1}{2} \rho \, U_\infty^2 ) / ( \frac{1}{2} \rho \, U_\infty^2 ), \text{ with } P_0 \text{ the front stagnation}$$
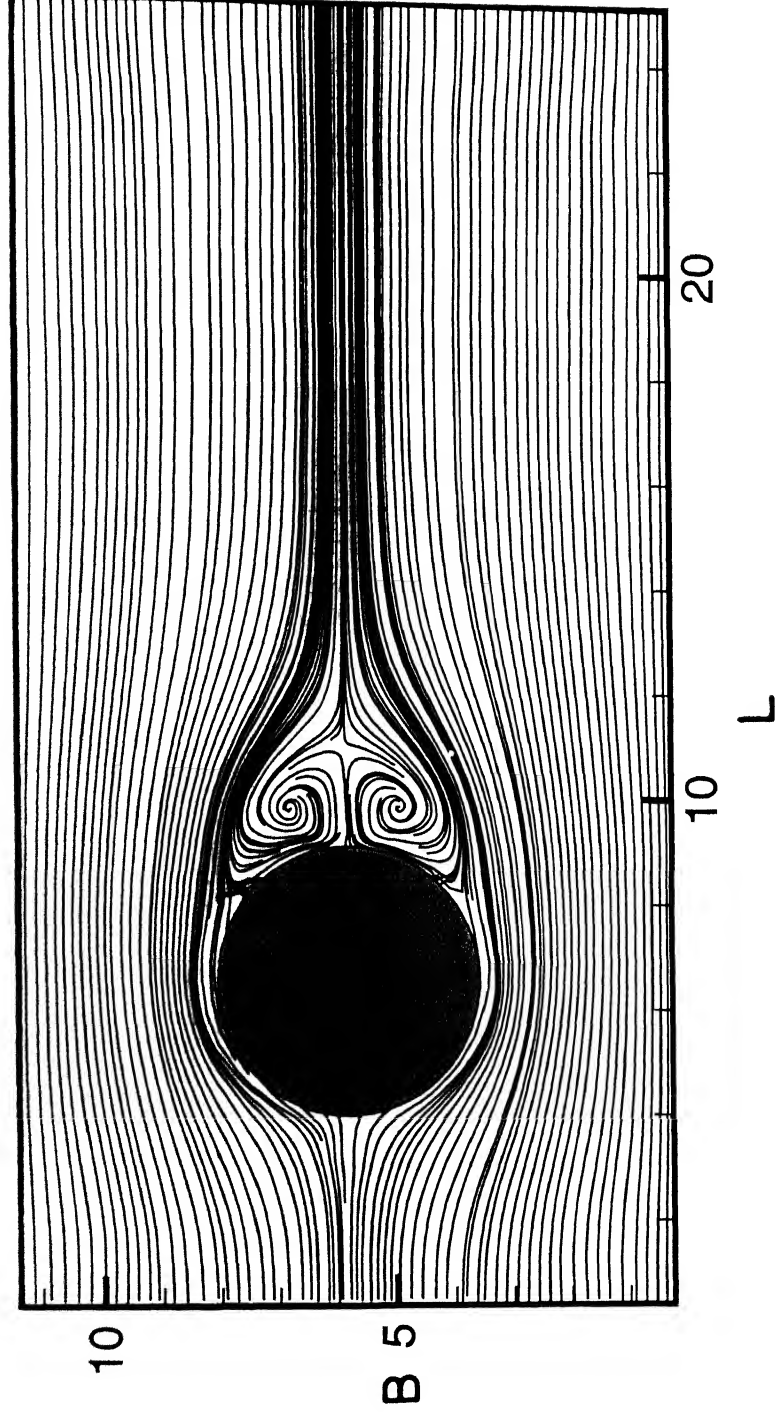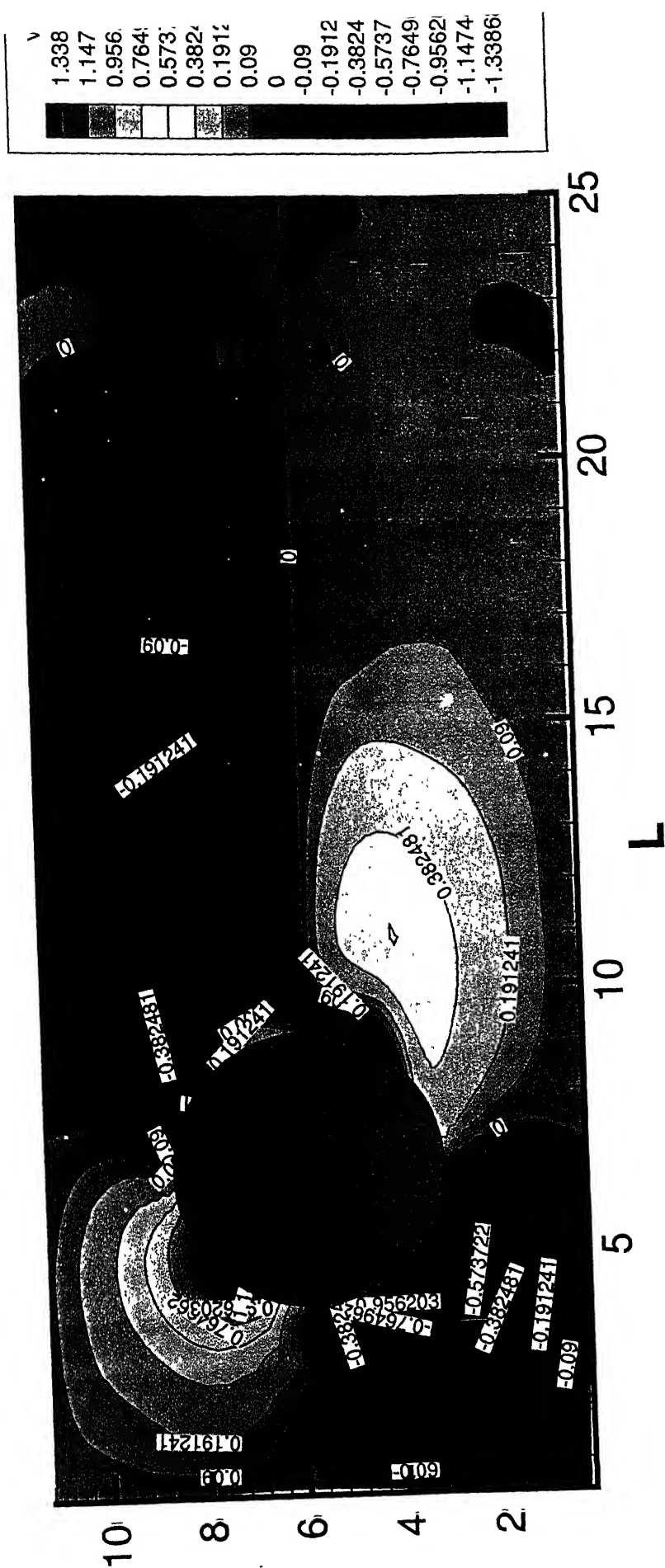
Streamlines on the horizontal midplane of the channel
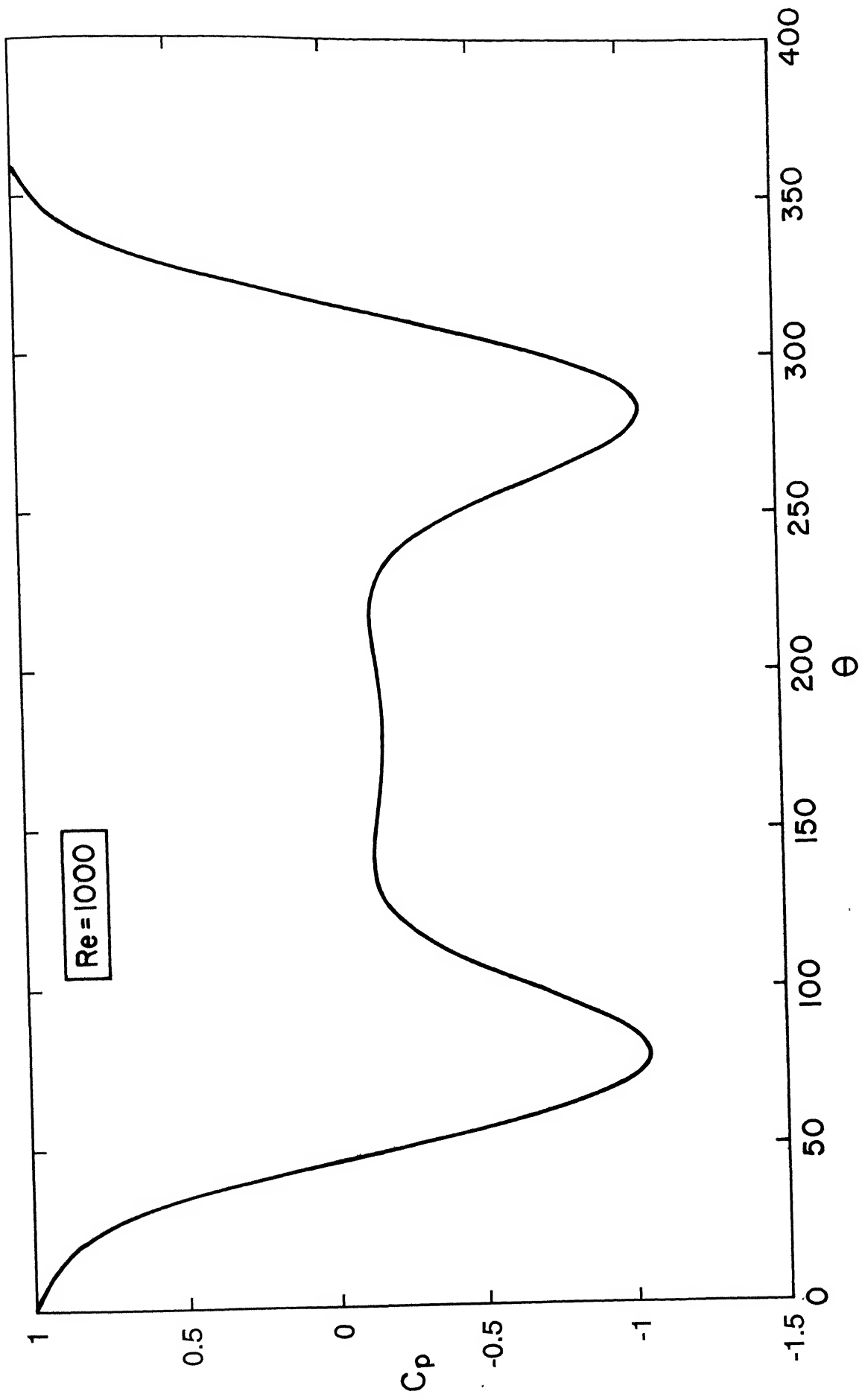Figure 5.2
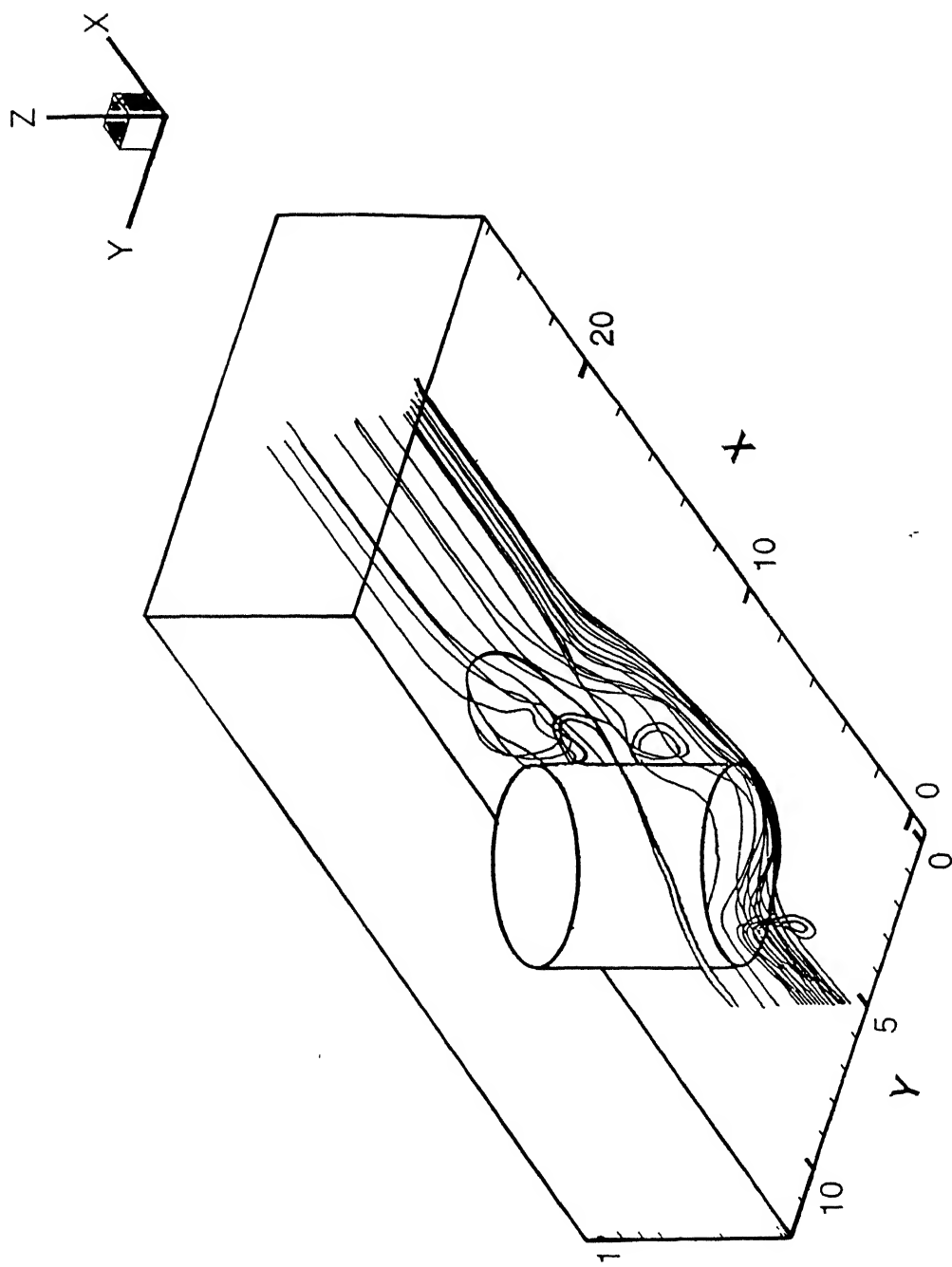
Structure of three-dimensional flow in a channel with a built-in circular
tube
Figure 5.3

Contour plot of time averaged axial velocity
Figure 5.4

Contour plot of mean transverse velocity
Figure 5.5

Time-averaged pressure distribution along the tube wall
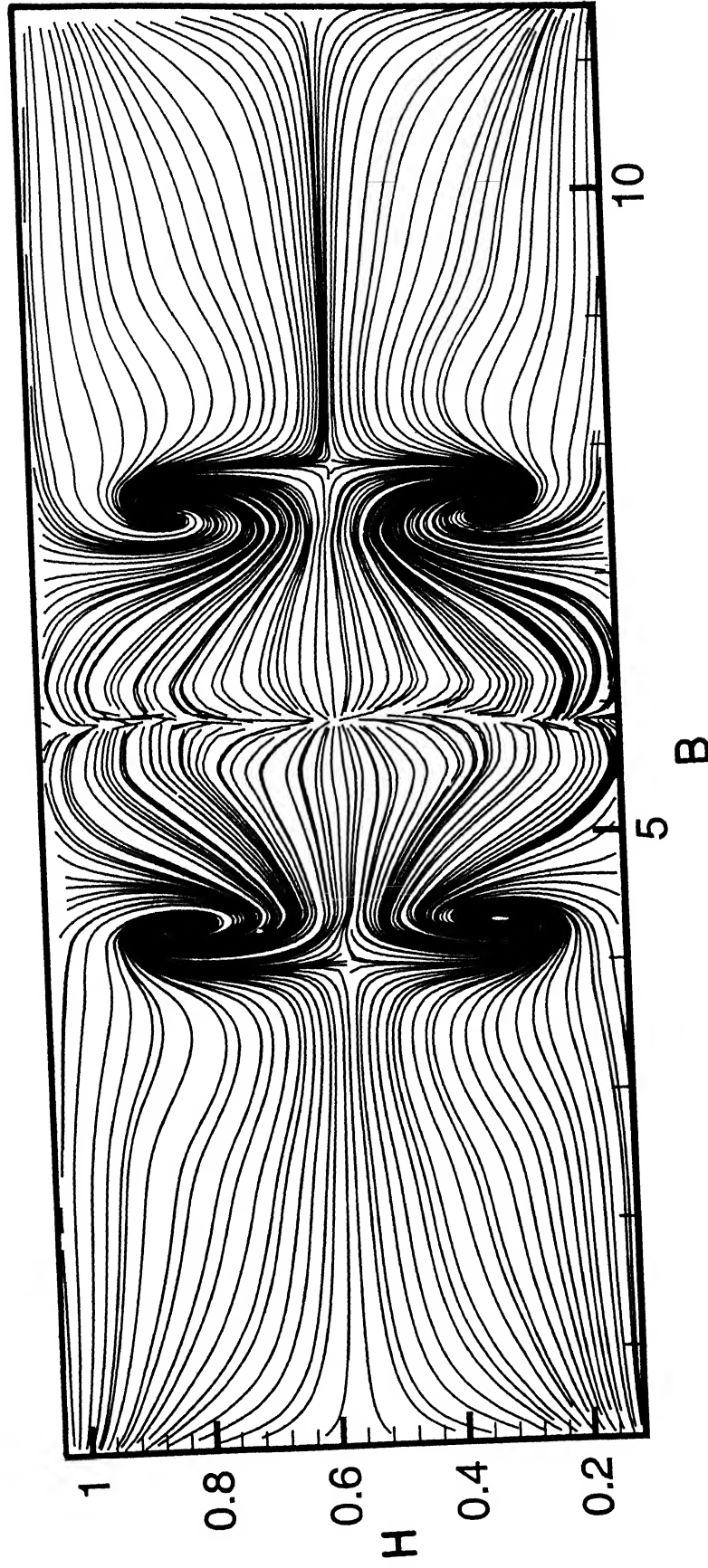Figure 5.6

point pressure. The incomplete pressure recovery due to the recirculation behind the cylinder is clearly observed in the figure.

Figure 5.7 shows the projection streamlines of the time averaged flow on the vertical midplane of the channel at $y = B/2$. The wake of the cylinder exhibits a strong three-dimensional behavior. The strong normal velocity component, $w$ is caused by the pressure gradient in the vertical direction in the wake region. This figure clearly shows the foot prints of the horseshoe vortices (marked as $S_1$ and $S_2$ in figure) and the reattachment line or the wake stagnation line (marked as $S_3$ in figure ).

Figure 5.8 shows the projection of streamlines of the time-averaged flow on the transverse plane located at a distance of 1.2 time the radius of the tube from the center of the tube. A complex structure is discerned on the transverse plane behind the tube. Flow near the leading edge of the tube describes the deviation from the two dimensional crossflow structure. Driven by the pressure gradient along the forward stagnation line of the tube, horseshoe vortices are formed in front of the tube. Two vortex systems, one at the junction of the top wall and tube and the other at the junction of the bottom wall and the tube, bend around the tube and form two sets of longitudinal vortex pairs. Kaul et al. (1985) describes the existence of the spiraling vortex systems, termed as the secondary vortex system, at the locations where the fluid is trapped between the end plates, tubes and the horseshoe vortices (also see Goldstein and Karni, 1984). As this secondary vortical flow filament on the bottom wall curls around the tube, it proceeds upward. The filament also begins to feel the effect of its counterpart coming
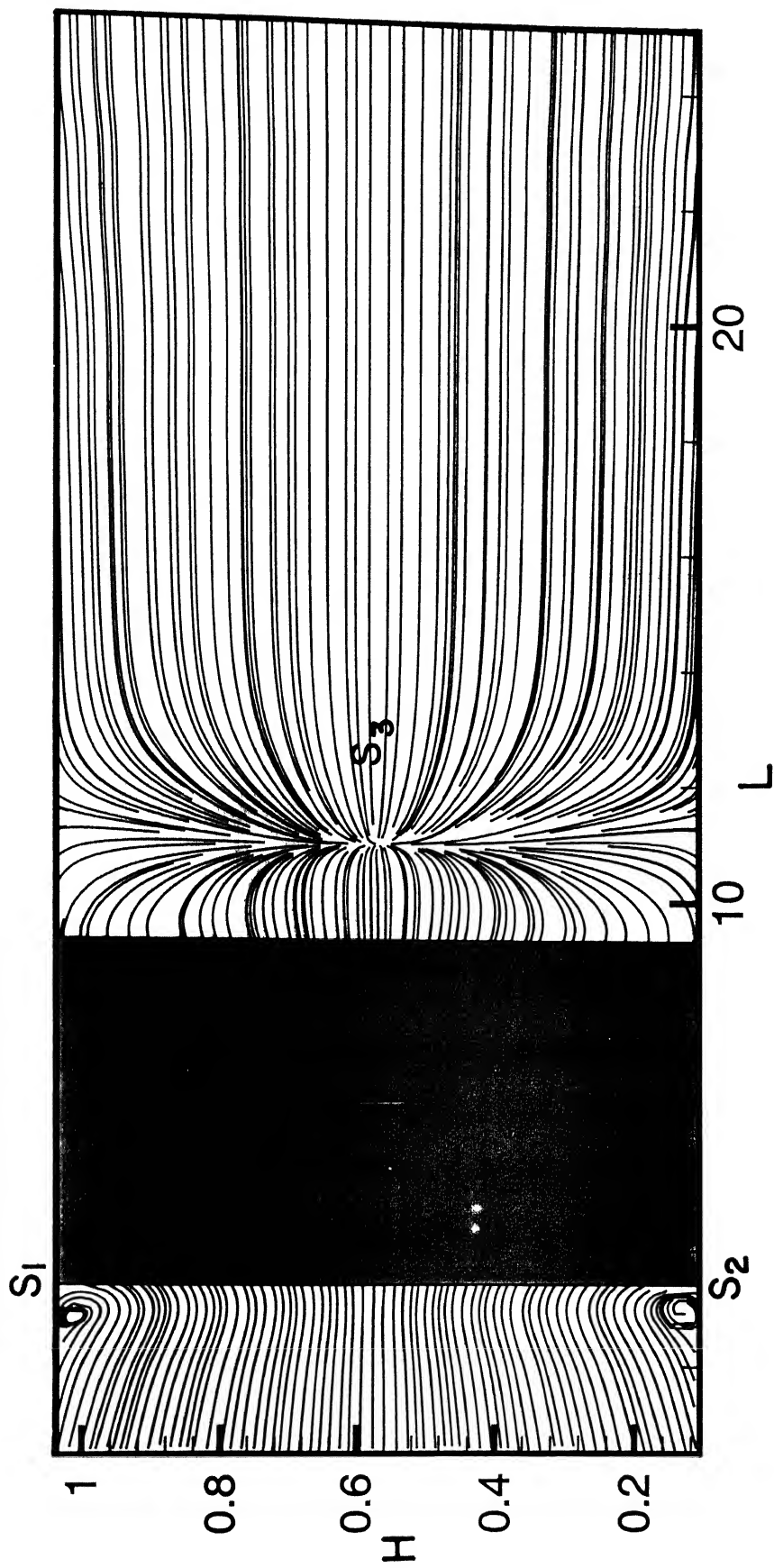
Streamlines on the vertical midplane of the channel
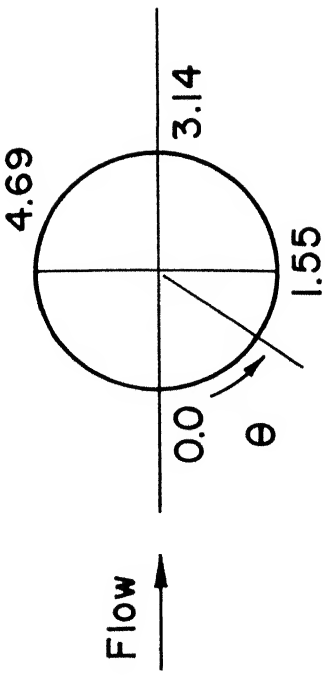Figure 5.7

The projected streamlines of the time averaged flow on the cross-stream plane located at a distance x/R = 1.2 from the center of the tube
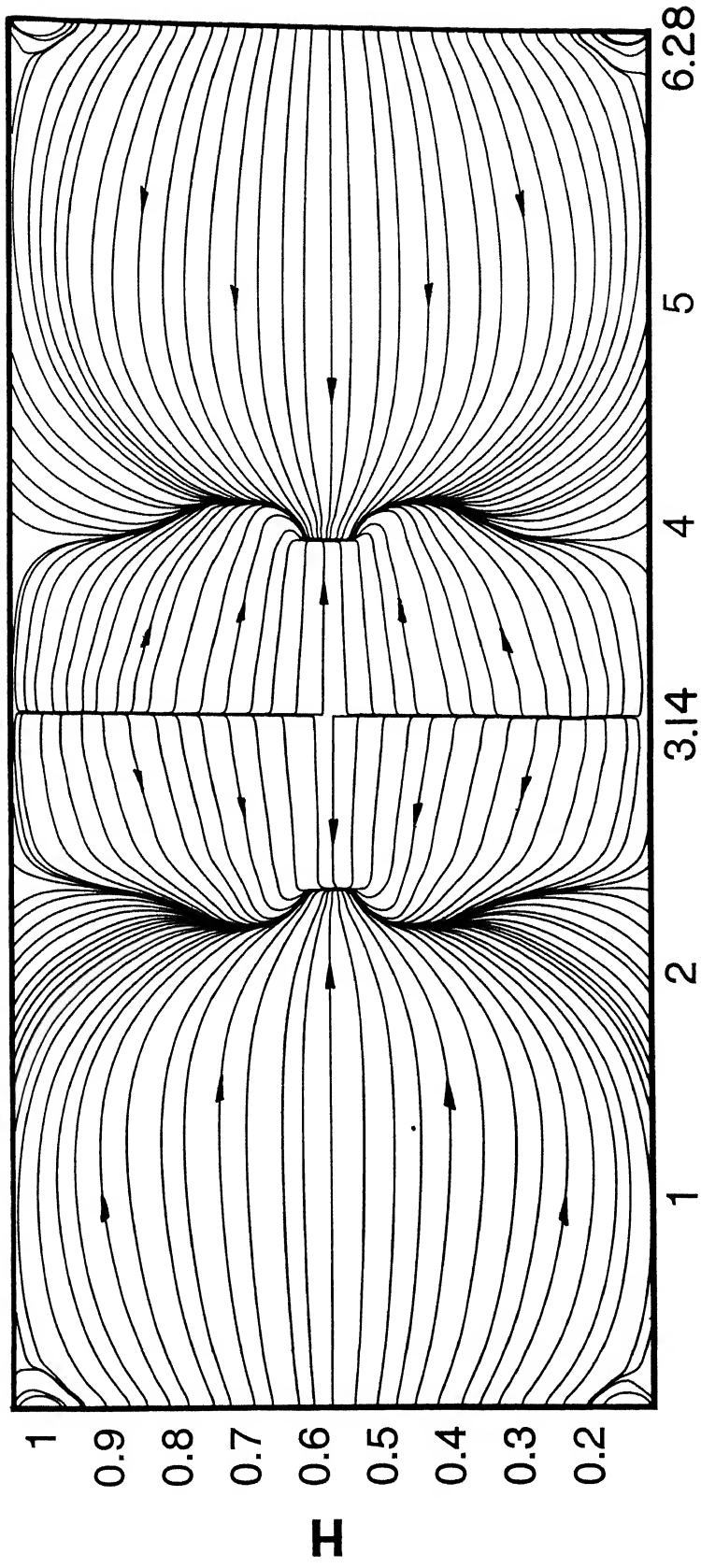
Figure 5.8

down from the top end wall. During their travel toward the symmetric midplane, the secondary vortex filaments interact with the horseshoe vortex systems and the vortex pair on both the walls get slightly shifted toward the symmetric midplane.

## 5.2.2 Limiting Streamlines on the Tube Surface and the Bottom Plate

The structure of the wall streamlines or limiting streamlines on the surface of the tube has investigated. This consists of the tangential components of velocity near the surface of the tube. The experimentalists have accomplished many investigations on the structure of limiting streamlines or the shear stresses lines on solid surfaces, but numerical computations are very few. Figure 5.9 shows such streamlines for the time-averaged flow. The mean flow field is symmetric so are the surface streamlines too. A bifurcation of the surface streamlines could be established. The bifurcation could be divided into two parts, a positive and negative bifurcation (Figure 5.10 (a) and (b)). The positive bifurcation takes place along the forward stagnation line at the surface of the tube. This line is characterized by a single line on the incoming stream surface, which bifurcates into two as the positive bifurcation line (Figure 5.10 (a)). This phenomenon of positive bifurcation can also be seen in Figure 5.9. The left, middle and the right parts of the Figure 5.9 represents the forward stagnation line of the tube at $\theta = 0$ and the line of reattachment at $\theta = \pi$. Figure 5.9, also reveals two other lines at an angle of $0.7\pi < \theta < 0.8\pi$ and
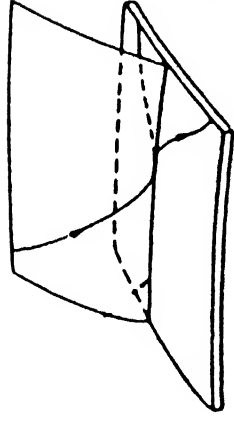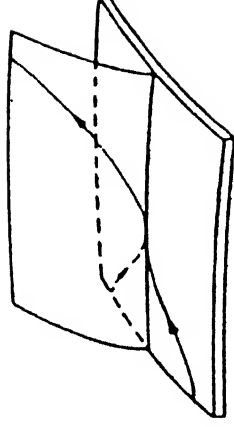
Limiting streamlines on the tube surface
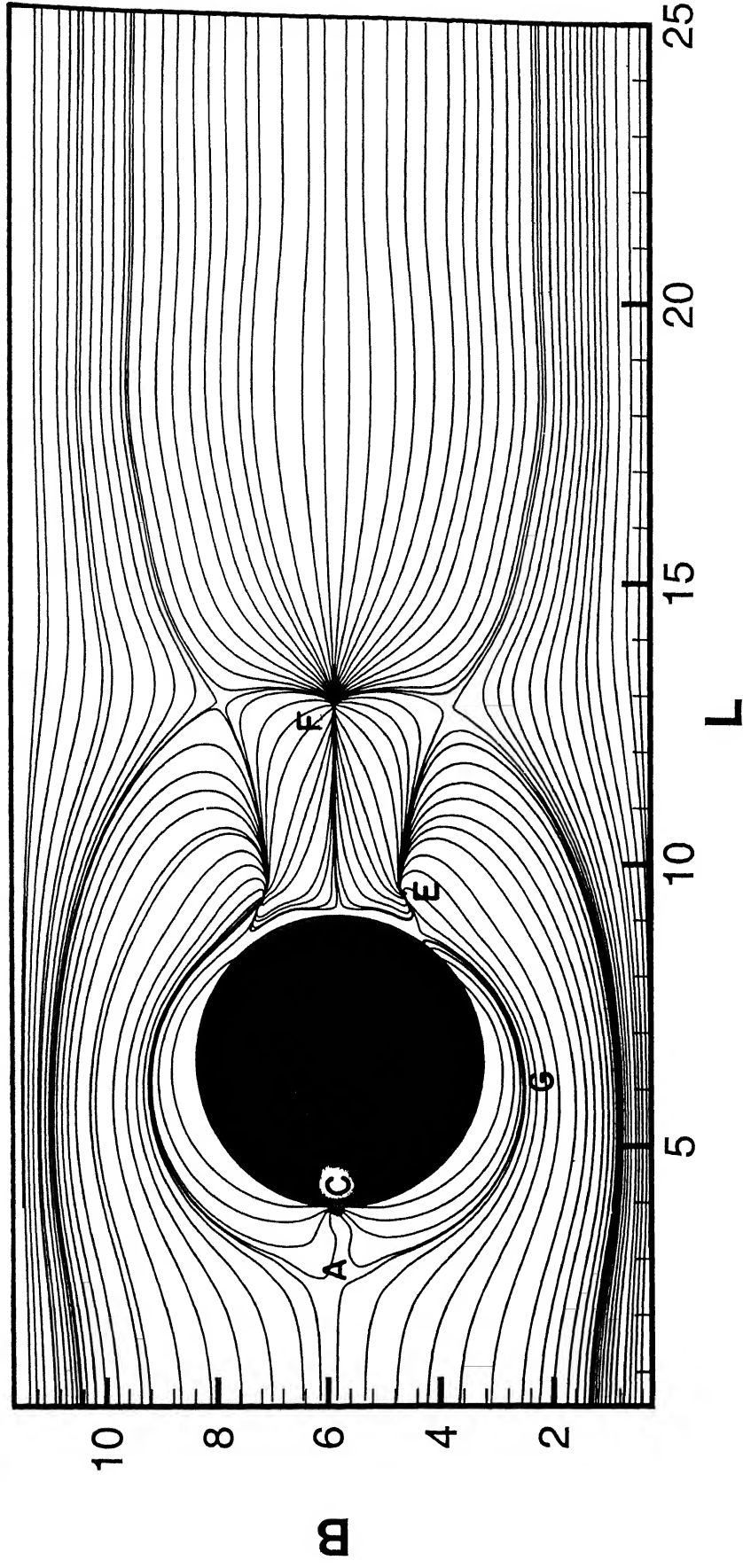Figure 5.9

Positive bifurcation

Negative bifurcation

Positive and negative bifurcation lines
Figure 5.10

$1.18\pi < \theta < 1.3\pi$ respectively. These are the lines where the components of the shear stress vector in the direction of $\theta$ are equal to 0. Hornung and Perry (1984) call this a negative stream surface bifurcation, which can also be seen in Figure 5.10 (b). Two streamlines combine to form a single streamline along the negative bifurcation line. These lines can be termed as separation lines along which the boundary layer separates from the tube surface. Figure 5.9 makes it obvious that the separation angle is small in the vicinity of the midplane of the tube and becomes larger in the vicinity of end walls, because of the greater flow speed in the plane of symmetry of the tube.

Figure 5.11 gives the streamlines of the time-averaged flow in the region close to the plate. A great deal of information about the flow and heat transfer characteristics can be extracted from this figure. A saddle point of separation and a horseshoe vortex system is observed from the figure. In Figure 5.11, the incoming flow does not separate in the traditional sense but reaches a stagnation or saddle point of separation (marked by A on the figure) and goes around the body. The nodal point of attachment (marked as C) and the separation lines which form circular arcs across the tube are clearly visible in the figure. The flow above the lower wall hits the front of the tube. A significant part of it moves downward and creates a region of reversed flow in front of the stagnation line. On each side of the tube, one finds a region of converging streamlines (marked as G). These are the traces of horseshoe vortex. Behind the body one finds two areas of swirling flow (marked as E) which are the footprints of an arch vortex. Finally, there is a wake stagnation point (marked F) further downstream of the body.

Limiting streamlines on the bottom plate
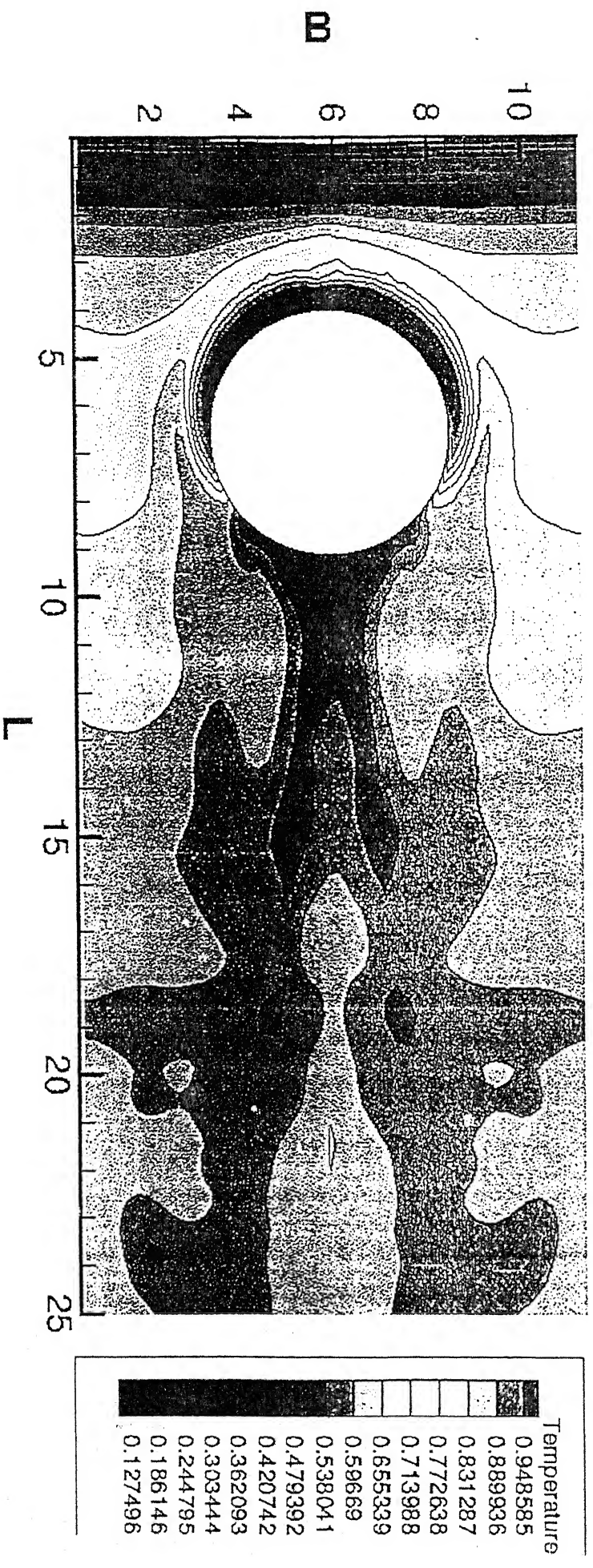Figure 5.11

# 5.3 Heat Transfer Characteristics

In this section a detailed study of heat transfer characteristics for the fin tube element (Figure 1.3) is presented. An effort has been made to understand the heat transfer characteristics on the basis of the flow pattern for the fin-tube heat exchanger module, which has been discussed in detail in previous section.
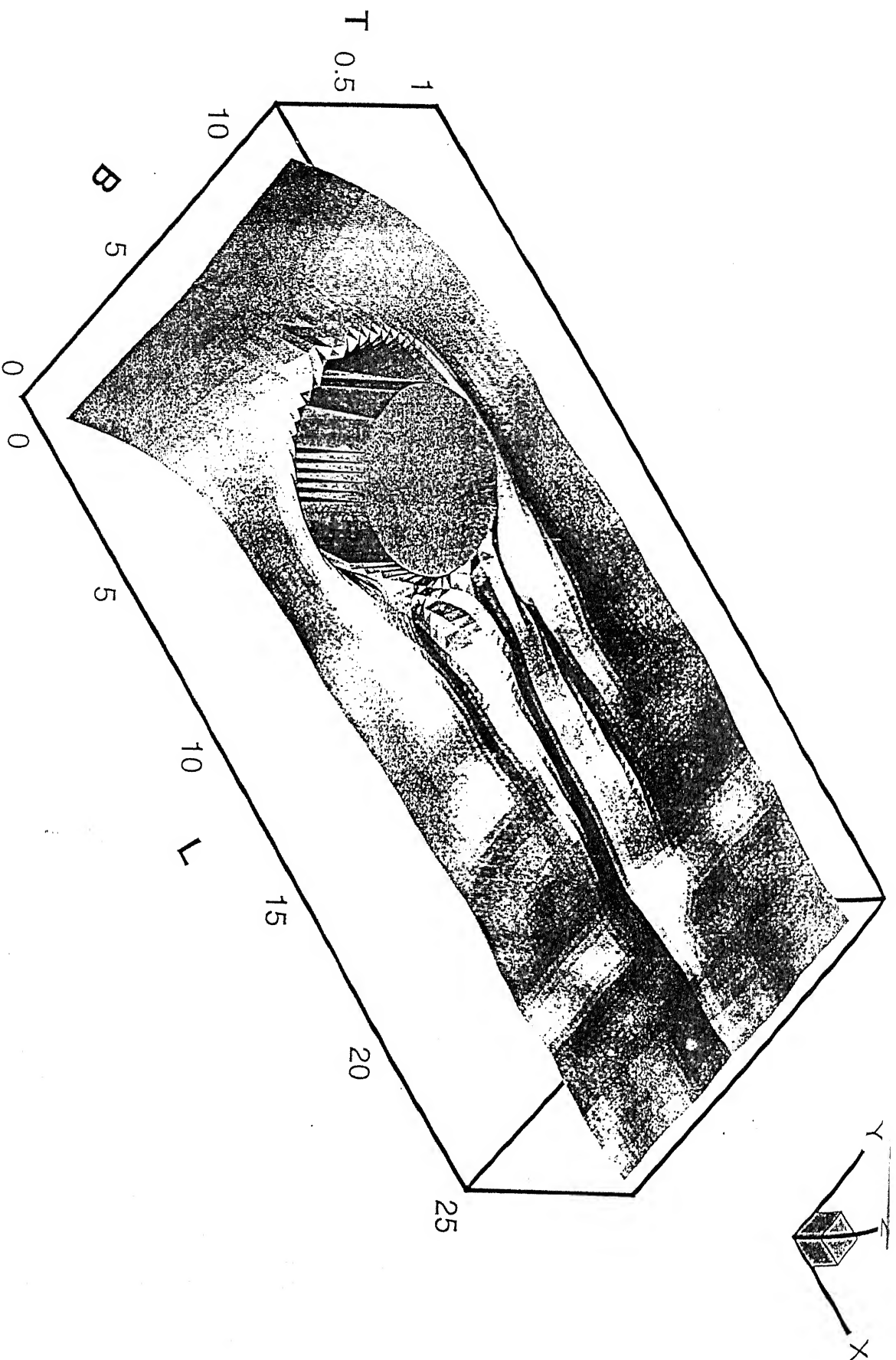
## 5.3.1 Temperature Distribution

Figure 5.12 shows the time-averaged temperature contours close to the bottom plate. Figure 5.13 shows the corresponding surface plot. The temperature field shows a dip near the forward stagnation line. This is due to the entertainment of cold fluid from the horizontal midplane of the channel. A high temperature in the wake region is also observed. In the wake region, the fluid recirculates with low velocity. Hence it gets heated more as compared to the neighboring regions. A low temperature is observed in a region wrapping the circumference of the tube. This is due to creation of the horseshoe vortices, which constitute the high-velocity spiraling motion of the fluid that sweeps cooler fluid from the outer regions of the thermal boundary layer toward the wall and consequently a low temperature is observed in this region.

Figure 5.14 shows the time-averaged temperature contours on the vertical midplane of the channel. The figure clearly reveals the thermal boundary layer development along the bottom plate. The contours, as expected, are

Temperature contours on the bottom plate

Temperature
0.948585
0.889936
0.831287
0.772638
0.713988
0.655339
0.59669
0.538041
0.479392
0.420742
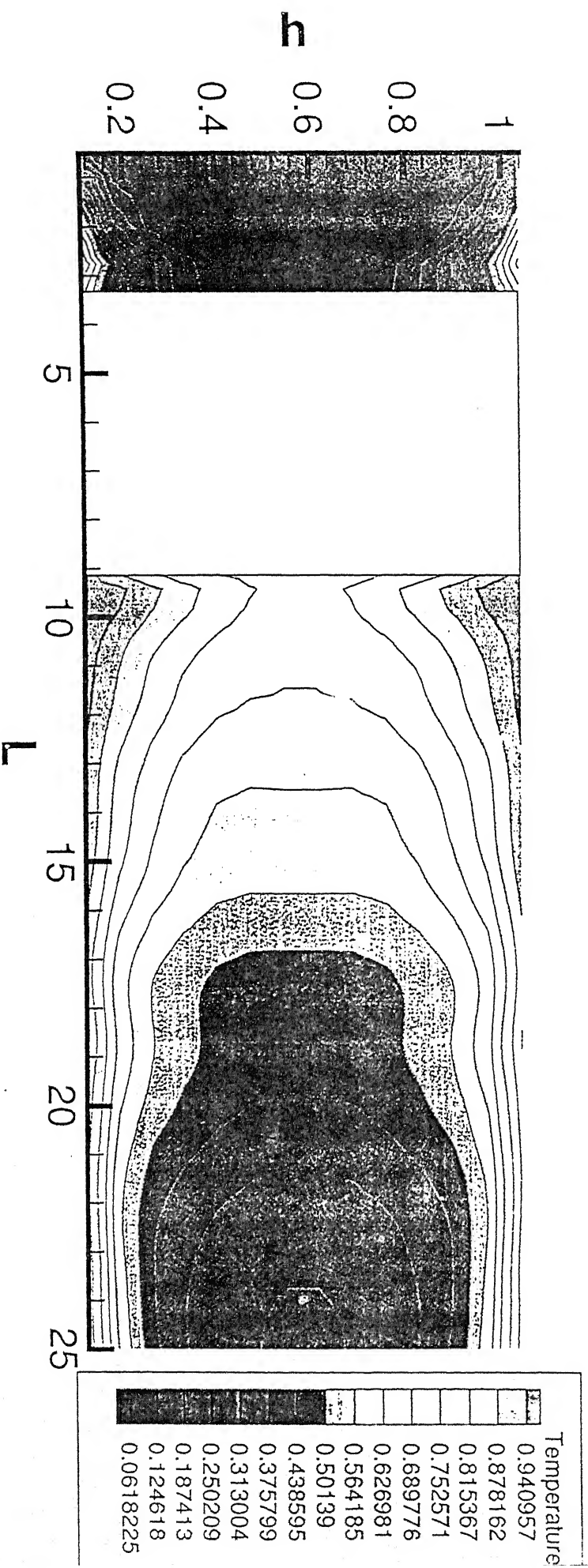0.362093
0.303444
0.244795
0.186146
0.127496

Time-averaged temperature contours close to the bottom plate
Figure 5.12

Time-averaged iso-surface for temperature close to the bottom plate
Figure 5.13

Temperature contours on the vertical midplane

Time-averaged temperature contours on the vertical midplane of the
channel
Figure 5.14

symmetric with respect to z=H/2. The gradients are clustered primarily in regions in front of the tube.

## 5.3.2 Nusselt Number and the Performance of the Heat Exchanger Module

Figure 5.15 shows the contour map of local Nusselt number obtained from the time-averaged temperature field for the bottom plate. Several interesting features are observed from the figure. Primarily follwing three regions may be distinguished. At the leading edge of the bottom plate, Nusselt number reaches its maximum and decreases gradually. At the leading edge, the cooler fluid comes in contact with the hot solid wall for the first time; hence the heat transfer is maximum. The gradual decrease in the Nusselt number is attributed due to the boundary layer development on the channel wall. This observation does not match with the experimental results of O'Brien et al. (2000) for the same Reynolds number. This is because in the experiment a flow development region was provided in the upstream of the test section. Consequently, in the experiment, the velocity boundary layer and the thermal boundary layer is approximately fully developed as it enters the test section. Present numerical simulation does not consider any flow development section. The uniform velocity and temperature profiles have been deployed in this study.

An abrupt increase of Nusselt number in front of the tube is observed. This results from the formation of horseshoe vortex system that consists of two

Isonusselt No. plot at the bottom plate
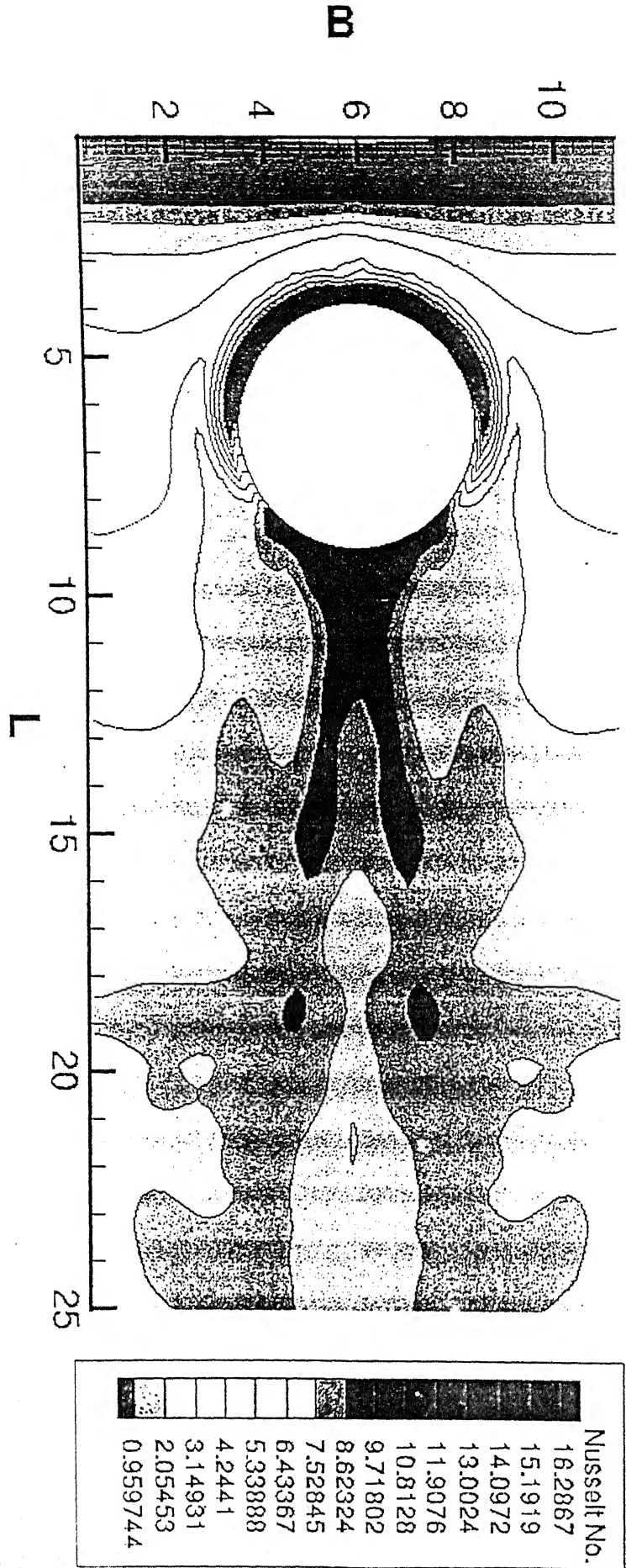
Contour map of local Nusselt number close to bottom plate

Figure 5.15

counter-rotating longitudinal vortices. As the fluid approaches the stagnation line of the circular tube, it slows down and its pressure increases. The smaller velocity in the boundary layer in the vicinity of the bottom plate, which supports the circular tube, leads to a smaller pressure increase. Thus, the induced pressure gradient causes the flow towards the bottom wall that interacts with the main stream. The fluid rolls up forming vortices, which finally wraps around the front half of the tube and extends to the rear of the tube, as shown schematically in Figure 5.16 (after Goldstein and Karni (1984). The spiraling motion of the horseshoe vortices brings about a better mixing and the heat transfer in this region is enhanced significantly. This is in good qualitative agreement with the experimental results presented by O'Brien et al. (2000). The quantitative comparisons have not been made because in experiments, the tube and the wall temperatures are not constant since both convective and conductive heat transfer take place from the tube and the wall. Present numerical simulation assumes the tube wall and fins to be at constant temperature. In addition, in the experiments, the sidewalls are no-slip walls whereas our simulation considers the sidewalls as the free-slip walls.

The Nusselt number is low in the wake region as shown in Figure 5.15. The poor heat transfer in this region is attributed to the separated dead water zone with fluid recirculating at a low velocity. This trend also matches qualitatively quite well with the experimental result of O' Brien et al. (2000).
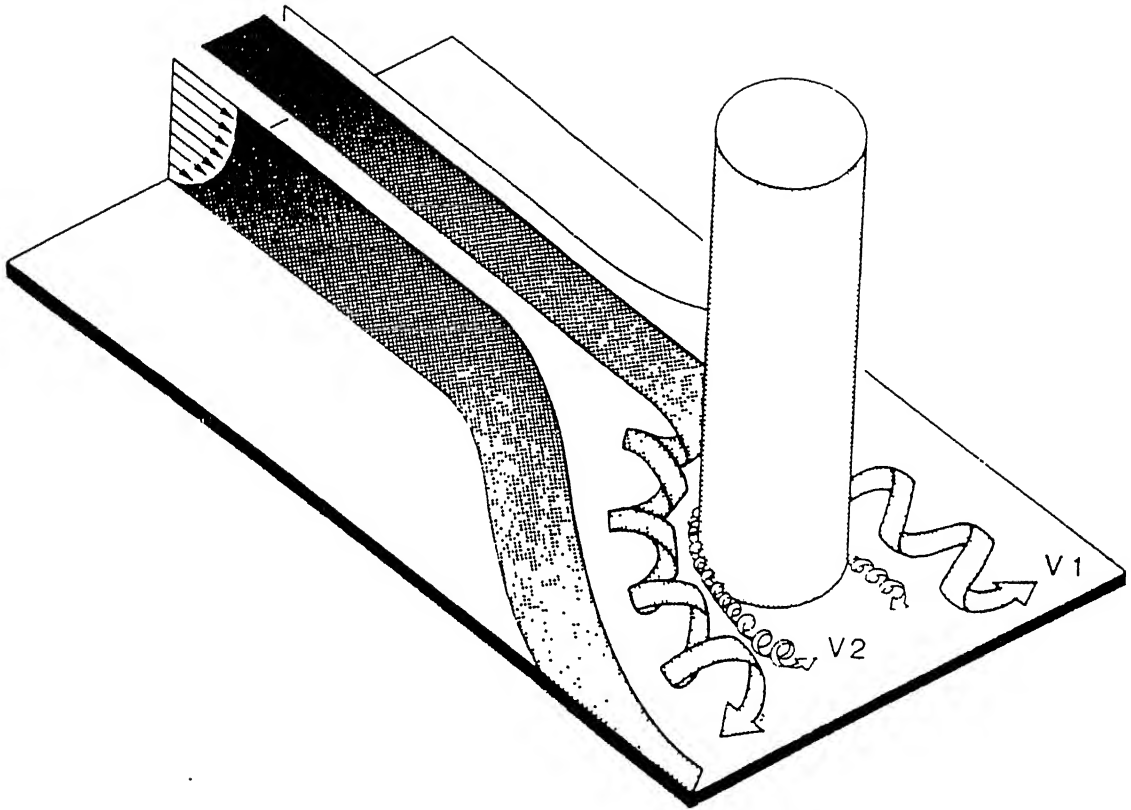
Three-dimensional boundary layer separation and horseshoe vortex
system in the region of interaction between mainstream boundary
layer and tube protruding from the wall( Goldstien and Karni (1984))
Figure 5.16

Figure 5.17 shows the distribution of span-averaged Nusselt number in the streamwise direction. At the leading edge of the fin, Nusselt number reaches its maximum and decreases gradually. There is an abrupt increase in Nusselt number in front of the tube. The reasons for this behavior are explained in this section.

Figure 5.18 represents the transverse variation in the local Nusselt number in the wake region at a distance of $x/R = 1.2$ from the center of the tube. The two peaks seen in the figure result from the downstream longitudinal bportion of the horseshoe vortices. The low heat transfer in the wake region $(-0.5 < y/R < 0.5)$ is clearly established from the figure.
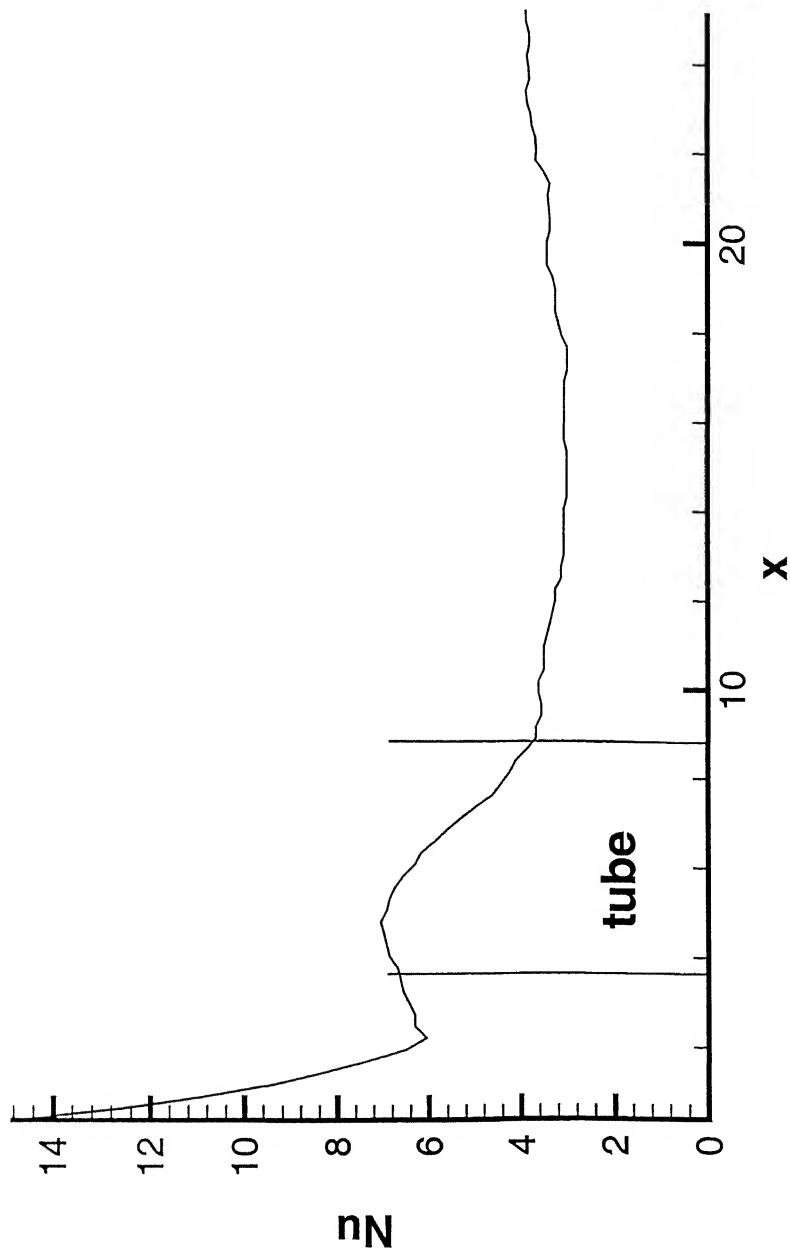
Span-averaged Nusselt number distribution in the streamwise
direction
Figure 5.17
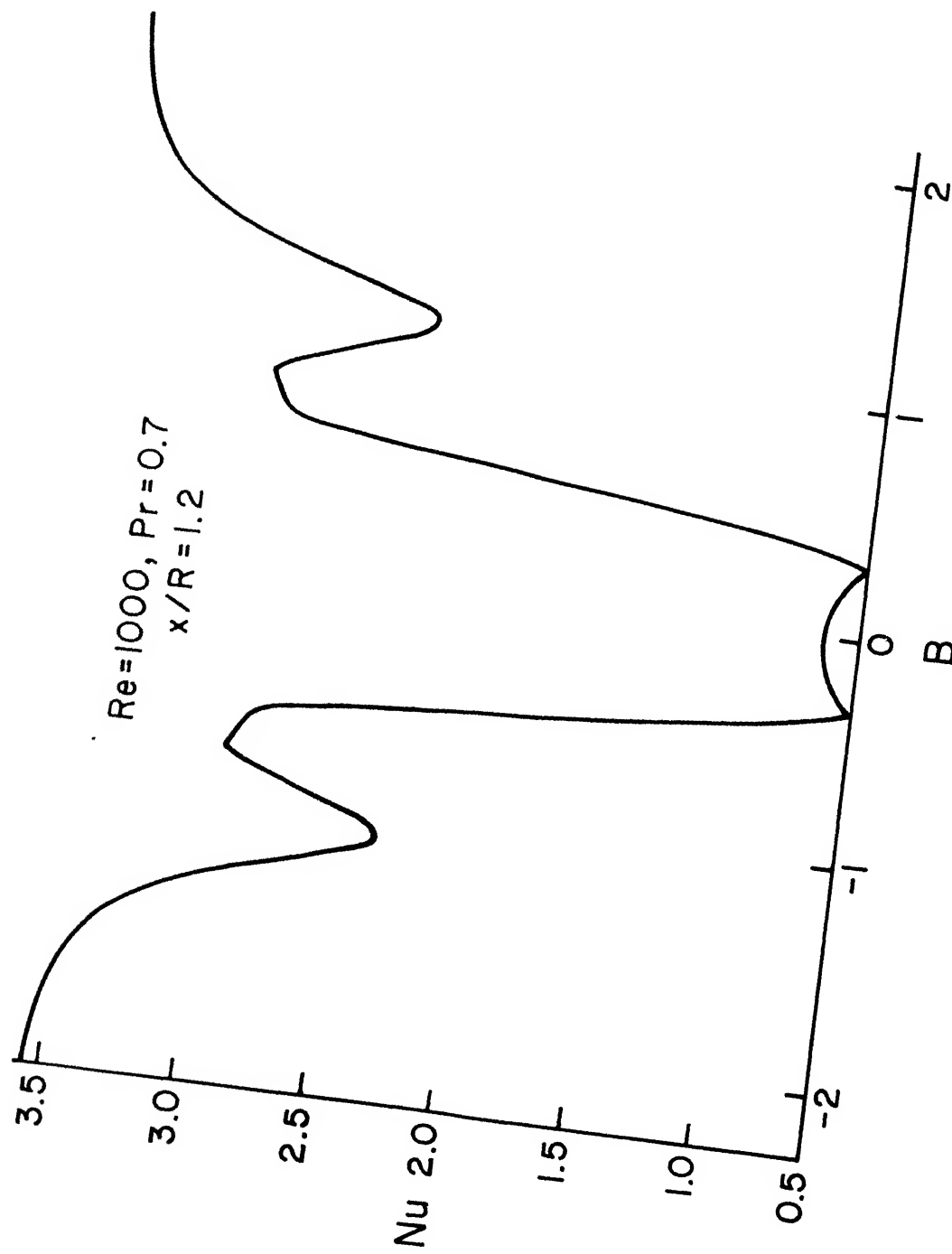
Transverse variation in the local Nusselt number in the near wake at a distance of x/R = 1.2 from the center of the tube

Figure 5.18

# Chapter 6

# Conclusion and Scope for Future Work

## 6.1 Conclusions

A three-dimensional numerical study on the flow and heat transfer characteristics in a narrow rectangular duct with a built-in circular tube in cross-flow has been performed. The duct was designed to simulate a passage, formed by two neighboring fins in a fin-tube heat exchanger. The governing conservation equations of fluid flow are derived in its integral form. An explicit control volume formulation devised by Eswaran and Prakash (1998) is used to solve the equations.

The flow field is completely different from the two dimensional flows. The third velocity component $w$ is surprisingly very large in the front and the near wake of the tube. In the rear of the tube it leads in accompaniment with the back flow to a screw-like motion of a helical vortex tube. Limiting streamlines on the tube surface have shown the typical separation lines. Limiting streamlines on the bottom wall have clearly established the presence saddle point of separation, the nodal point of attachment in front of the tube-bottom wall junction and the horseshoe vortex system that wraps around the tube and extend to the rear of the tube. The separation line

emanating from the saddle point is also clearly established. The local span-averaged Nusselt number and the iso-Nusselt number distribution clearly establish the high heat transfer near the leading edge of the fins and in the region influenced by the horseshoe vortex. The poor heat transfer in the dead water zone is observed. A double peak in local fin-surface heat transfer in the stagnation region is clearly observed. Although no quantitative comparisons can be made with the available experimental results of O'Brien (2000) because of the different flow and geometric conditions, the qualitative comparisons are meaningful and it matches quite well with experimental results.

## 6.2 Scope for Future Work

The results of this work validate three-dimensional unsteady flow models as a useful technique in improving the heat transfer efficiency for air-cooled heat exchangers. As the results reveal, regions of relatively high heat transfer are constrained to small regions just upstream and to the sides of the tube and in the immediate vicinity of the horseshoe vortices downstream of the tube. The heat transfer performance can be improved by placing a delta winglet pair behind the tube. The winglet pair can be mounted following two different arrangements. The conventional way of placing the winglet pair is such that the transverse distance between the leading edges is less than the transverse distance between the trailing edges. Since the vortical structure due to such an arrangement shows common flow in the direction of the wall (bottom plate of the channel), the configuration is called 'common flow down'. However, Torii et al. (2000) have suggested a special arrangement of

placing the winglets behind the circular tube. In this arrangement, the distance between the trailing edges of the winglet pair is less than the distance between the leading edges. The vortical structure entails common flow away from the wall in such an arrangement. Hence the configuration is called 'common flow up'. The salient feature of this arrangement is creation of a virtual constriction of the flow passage near the rear stagnation point of the tube. This constriction brings about considerable separation delay and reduces form drag. Due to the accelerating stream, the poor heat transfer zone in the wake of the cylinder is removed. The future investigations with the winglet pair should include both the configurations, such as 'common flow down' and common flow up'. Biswas and Mitra (1988) have conducted comparative study using delta winglet pair and the rectangular winglet pair as the vortex generators. As a future computational study both delta winglet pair and rectangular winglet pair can be used and the condition for the optimum heat transfer can be determined.

# References

Achaichia, A.,and Cowell, T.W.,1998, Heat Transfer and Pressure Drop Characteristics of Flat Tube and Louvered Plate Fin Surfaces, *Experimental Thermal and Fluid Science*, Vol. 1, pp.147-157.

Acharya, S., Myrum , T.A. ,and Inamdar, S., 1991, Subharmonic Excitation of the Shear Layer  Between Two Ribs: Vortex  Interaction and Pressure Field, AIAA J., Vol. 29, pp. 1390-1399.

Amon,C.H., and Patera, A.T., 1989, Numerical Calculation of Stable Three-Dimensional Tertiary States in Grooved-Channel Flow, *The Phys. Fluids*-A, Vol. 1, No.12, pp. 2005-2009.

Biswas, G. and Chattopadhyay, H., 1992, Heat Transfer in a Channel with Built-In Wing-Type Vortex Generators , *Int. J. Heat and Mass Transfer*, Vol. 35, pp. 803-814.

Biswas, G. and Mitra, N.K., 1998, Longitudinal Vortex Generators for Enhancement of Heat Transfer in Heat Exchanger Applications, *Proc. 11th Int. Heat Transfer Conference*, Kyongju, Vol. 5, pp. 339-344

Biswas, G., Mitra, N K., and Fiebig , M , 1994, Heat Transfer Enhancement in Fin-Tube Heat Exchangers by Winglet-Type Vortex Generators, *Int. J. Heat Mass Transfer*, Vol.35, pp. 803-814.

Braza, M., Chassaing, P., and Ha-Minh , H., 1986, Numerical Study and Physical analysis of the Pressure and Velocity Fields in the Near Wake of a Circular Cylinder, *J. Fluid Mech.* , Vol. 165, pp. 79-130.

Chorin, A.J., 1967, A Numerical Method for Solving Incompressible Viscous Flow Problems , *J. Comp. Phys.*, Vol. 2, pp. 12-26.

Dong, Y., 1989, Experimentelle Untersuhung der Wechselwirkung von Langswirbelerzeugern und Kreiszylindern in Bezungauf Warmeubergang und Stromungsverlust, Doctoral Thesis, Ruhr-Universtat Bochum, Germany.

Eibeck, P.A. and Eaton, J.K, 1987, Heat Transfer Effects of a Longitudinal Vortex Embedded in a Turbulent shear Flow, *Journal of Heat Transfer*, Vol. 109, pp. 16-24.

Eswaran, V., Biswas, G., Muralidhar, K. and Dhande, S.G., 1995, Numerical Simulation of Unsteady Three-Dimensional Flow around an Elongated Body Moving in an Incompressible Fluid, Internal Report, IIT Kanpur.

Eswaran, V., and Prakash, S., 1998, A Finite Volume Method for Navier-Stokes Equations, *Proceedings of the Third Asian CFD Conference, Bangalore,* Vol. 1, pp. 127-133.

Fiebig, M., Kallweit, P. and Mitra, N.K., 1986, Wing Type Vortex Generators For Heat Transfer Enhancement, *Proceeding of the Eighth Int. Heat Transfer Conference*, San Francisco, Vol. 6, pp. 2909-2913.

Fiebig, M., Brockmeier, U., Mitra, N.k., and Guntermann, T., 1989, Structure of Velocity and Temperature Fields in Laminar Channel Flows with Longitudinal Vortex Generators, *Numerical Heat Transfer-Part A*, Vol.15, pp. 281-302.

Fiebig, M., Kallweit, P., Mitra, N. k., and Tiggelbeck, S., 1991, Heat Transfer Enhancement and Drag by Longitudinal Vortex Generators in Channel Flow, *Experimental Thermal and Fluid Science*, Vol. 4, pp. 103-114.

Fletcher, C.A.J., 1988, <u>Computational Techniques for Fluid Dynamics</u>, Vol.1, ( Fundamentals and General Techniques ), Springer Verlag.

Garg, V.K., and Maji, P.K., 1987, Flow through a Converging-Diverging Tube with Constant Wall Enthalpy, *Numerical Heat Transfer,* Vol. 12, pp. 285-305.

Ghaddar, N.K., Korczak, K.Z., Mikic, B.B., and Patera, A.T., 1986a, Numerical Investigation of Incompressible Flow in Grooved Channels, Part 2- Stability and Self-Sustained Oscillations, *J. Fluid Mech.*, Vol. 163, pp. 99-127.

Ghaddar, N.K., Magen, M., Mikic, B.B , and Patera, A.T., 1986b, Numerical Investigation of Incompressible Flow in Grooved Channels, Part 1- Resonance and Oscillatory Heat-Transfer enhancement, *J. Fluid Mech.*, Vol. 168, pp. 541-567.

Goldstein, R.J and Karni.J, 1984, The effect of a wall boundary layer on a local mass transfer from a cylinder in crossflow, *J. Heat Transfer*, Vol. 106, pp. 260-267.

Harlow, F.H. and Welch, J.E., 1965, Numerical Calculation of Time-dependent Viscous Incompressible Flow of Fluid with Free Surface, *The Phys. Fluids,* Vol. 8, pp. 2182-2188.

Harlow, F.H. and Amsden, A.A., 1970, The SMAC Method : A Numerical Technique for Calculating Incompressible Fluid Flows, Los Almos Scientific Lab. Rept., LA 4370.

Hirt, C.W. and Cook, J.L., 1972, Calculating Three-Dimensional Flows around Structures and over Rough Terrain,*J.Comp.Phys.*, Vol. 10, pp. 324-340.

Horung, H., Perry, A. E., 1984, Some aspects of three-dimensional separation, Z.f. Flugwissenschaften u. Weltraumforschg., 8-2,3, pp. 77-87 and pp. 155-160.

Hummel, D., and Srinivasan, P.S., 1967, Vortex Breakdown Effects on the Low-Speed Aerodynamic Characteristics of Delta Wings in Symmetrical Flow, *J.Roy. Aero. Soc.*, Vol. 71, pp. 319-322.

Hummel,.D., 1973, Study of the Flow Around Sharp-Edges Slender delta Wings with Large Angles of Attack, NASA TTF-15, Vol. 107.

Issa, R.I, Gosman, A.D. and Watkins A.P ,1986, The Computation of Compressible and Incompressible Recirculating Flows by a Non-Iterative Implicit Scheme, *J.Comp.Phys.*, Vol. 63, pp. 66-82.

Jang, D.S., Jetli, R., and Acharya, S., 1986, Comparison of PISO, SIMPLER and SIMPLEC Algorithms for the Treatment of the Pressure Velocity Coupling in Steady Flow Problems, *Numerical Heat Transfer*, Vol 10, pp. 209-228.

Kaul , U.K., Kwak, D., and Wagner, C.,1985, Computational Study of Saddle-Point Separation and Horeshoe Vortex System, AIAA J.,Paper 85-0812, Reno,Nev.

Kim, S.W., and Benson, T.J., 1992, Comparison of SMAC, PISO and Iterative Time-Advancing Schemes for Unsteady Flows, *Computers and Fluids,*Vol. 21, pp. 435-454.

Khosla, P.K., and Rubin, S.G., 1974, A diagonally dominant second-oder accurate implicit scheme, *Computers and Fluids,* Vol. 2, pp. 207-209.

Kobayashi, M.H., and Pereira, C.F., 1991, Calculation of Incompressible Laminar Flows on a Non-Staggered, Non-Orthogonal Grid, *Numerical Heat Transfer*, Part-B, Vol.19, pp. 243-262.

Legendre, R., Separation de courant lecoulement laminaire tridimensional, 1956 *Recherches Aero*, Vol 54, pp. 3-8,.

Lighthill, M., <u>Attachment and Separation in three-dimensional flow, in laminar boundary layers, ed</u>. L. Rosenhead, 1963, Vol 2, pp. 72-82, Oxford University Press.

Majumdar, S., 1988, Role of Underrelaxation in Momentum Interpolation for Calculation of Flow with Nonstaggered Grids, *Numerical Heat Transfer*, Vol. 13, pp. 125-132.

Majumder, D., and Amon, C.H., 1992, Heat and Momentum Transport in Self-Sustained Oscillatory Viscous Flows, *Journal of Heat Transfer,* Vol.114, pp. 886-873.

Mukhopadhyay, A., Sundarajan, T., and Biswas, G., 1993, An Explicit Transient Algorithm for Predicting Incompressible Viscous Flows in Arbitary Geometry, *Int. J. Numerical Methods Fluids*, Vol. 17, pp. 975-993.

Myrum, T.A., Achrya, S., Inamdar, S., and Mehrotra, A, 1992, Vortex Generator Induced Heat Transfer Augmentation Past a Rib in a Heated Duct Air Flow, *Journal of Heat Transfer,* Vol. 114, pp. 280-284.

Nicholas, B.D., and Hirt, C.W., 1971, Improved Free Surface Boundary Conditions for Numerical Incompressible Flow Calculations, *J.Comp.Phys.,* Vol. 8, pp. 434-448.

Orlanski, I., 1976, A Simple Boundary Condition for Unbonded flows, *J. Comp Phys*, Vol. 21, pp. 251-269.

O'Brien, J.E., Sohal, M.S., Sohal, 2000, August 20-22 Proceedings of NHTC'00 34th *National Heat Transfer Conference Pittsburgh, Pennsylvania.*

Patankar , S.V. and Spalding , D.B., 1972, A Calculation Procedure for Heat Mass and Momentum Transfer in Three-Dimensional Parabolic Flows, *Int.J.Heat Mass Transfer*, Vol. 15, pp. 1787-1806.

Patankar , S.V., 1981, A Calculation Procedure for Two-Dimensional Elliptic Situations, *Numerical Heat Transfer*, Vol. 4, pp. 409-425.

Pearcy , H.H , 1961, <u>Shock-Induced Separation in Boundary Layers, in Boundary Layers and Flow Control,</u> Vol. 2, Pergamon Press, New York.

Peric, M., 1985, A Finite Volume Method for the Prediction of Three-Dimensional Fluid Flow in Complex Ducts, Ph.d, Thesis, University of London.

Rhie, C.M., 1981, A Numerical Study of the Flow Past an Isolated Airfoil with Separation, PhD. Thesis, Dept of Mechanical and Industrial Engineering, University of Illinios at Urbana Champaign, 1981.

Rhie, C.M., and Chow, W.L., 1983, Numerical Study of the Turbulent Flow Past an Airfoil with Trailing Edge Separation, AIAA J., Vol. 21, pp. 1525-1532.

Robichaux, J., Tafti, D.K., and Vanka, S.P., 1992, Large-Eddy Simulations of Turbulence on the CM-2, *Numerical Heat Transfer*, Part-B, Vol. 21, pp. 367-388.

Thomas, J. L., Krist, S. T., and Anderson, W. K., 1990, Navier Stokes Computation of Vertical Flows over Low-Aspect-Ratio Wings, AIAA J., Vol. 28, pp. 205-212.

Tiggelbeck, S., Mitra, N.K., and Fiebig, M., 1992, Flow Structure and Heat Transfer in a Channel with Multiple Longitudinal Vortex-Generators, *Experimental Thermal and Fluid Science*, Vol. 5, pp. 425-436.

Torii, K., Nishino, K., Kwak, K.M. and Kawai, R., 2000, YNU Team Report: Research Results and Implementation Plan, NEDO VORTEX Team Meeting, October 5-6.

Valencia, A., 1992, Warmeubergang und Druckverlust in Lamellen-Rohr-Warmeubertragen mit Langsurbelerzugern, Doctoral Thesis, Ruhr-Univesitat Bochum, Germany.

Van Doormal, J.P., and Raithby, G.D., 1984, Enhancements of the SIMPLE method for Predicting Incompressible Fluid Flows, *Numerical Heat Transfer,* Vol. 7, pp. 147-163.

Vanka, S.P., 1987, Second-Order Upwind Differencing in a Recirculating Flow, AIAA J., Vol. 25, pp. 1435-1441.

Velusamy, K., and Garg, V.K., 1993, Entrance Flow in Elliptic Ducts, *Int. J. Numer. Methods Fluids,* Vol. 17, pp. 1079-1096.

Vicelli, A.J., 1971, A Computing Method for Incompressible Flows bounded by Moving Walls, *J. Comp. Phys.,* Vol. 8, pp. 119-143.

Webb, B.W., and Ramadhyani, S., 1985, Conjugate Heat Transfer in a Channel with Staggered Ribs, *Int. J. Heat Mass Transfer,* Vol. 28, pp. 1679-1687.

# <u>Appendix</u>

## Attachment and separation in three-dimensional flows

At a very small normal distance z from the solid surface,

$$\left(\frac{\partial u}{\partial z} \sim \frac{u}{z}, \frac{\partial v}{\partial z} \sim \frac{v}{z}\right) \text{so}$$

$$\vec{V} = \vec{\varepsilon}_w z \qquad\qquad\qquad\qquad \text{(A-1)}$$

$$\text{where } \vec{\varepsilon}_w = \left(\frac{\partial u}{\partial z}, \frac{\partial v}{\partial z}\right) = \frac{\vec{\tau}_w}{\mu} \qquad\qquad \text{(A-2)}$$

where, $\vec{\tau}_w$ represents the skin friction vector field.
From (A-1) we have,

$$u = \varepsilon_x z, \quad v = \varepsilon_y z \qquad\qquad\qquad \text{((A-3)}$$

for solenoidal flow field

$\text{div}\,\vec{q} = 0$ where $\vec{q} = (u, v, w)$

or, $\dfrac{\partial w}{\partial z} = -\Delta z$, where $\Delta = div\,\vec{\varepsilon}_w$

On integrating we have

$$w = \frac{-1}{2}\Delta z^2 \qquad\qquad\qquad\qquad \text{(A-4)}$$

from equation (A-4) it is obvious that streamlines very close to the surface will be parallel to the surface (w=0) provided $\vec{\varepsilon}_w \neq 0$

**Critical Points:** Critical points are those where $\vec{\varepsilon}_w = 0$ or the velocity vector vanishes, therefore its directions are indeterminate.

**Separation Points:** are those points where the vertical (normal) component of velocity w>0

If $w > 0$ from equation (A-4) we have $\Delta < 0$, i.e. the divergence of skin friction vector is negative at the separation point.

**Attachment Point**: are those points where the normal component of velocity w<0

$$w < 0, \quad or \quad \Delta > 0 \tag{A-5}$$

The divergence of skin friction vector is positive at the attachment point.

**Skin Friction Lines**: are curves such that tangent at any point give direction of the $\vec{\varepsilon}_w$ or the skin friction vector field at that point.

From equation (A-1) it is obvious that for the location very close to the surface, streamlines lie closely along with the skin friction lines.

Critical Points can be divided primarily of two types, Saddle points and nodal points. The nature of the critical point depends on the Jacobian of the shear stress vector $(\vec{\varepsilon}_w)$ and the divergence of the skin friction vector field.

**Saddle Points:** For any initial point in the neighborhood of this critical point, with passage of time, there will be attraction towards this point along one direction and repulsion from this point along another direction.

**Mathematically**

$$J = \left( \frac{\partial(\varepsilon_x, \varepsilon_y)}{\partial(x, y)} \right)_{(x_0, y_0)} = \begin{vmatrix} \dfrac{\partial \varepsilon_x}{\partial x} & \dfrac{\partial \varepsilon_x}{\partial y} \\ \dfrac{\partial \varepsilon_y}{\partial x} & \dfrac{\partial \varepsilon_y}{\partial y} \end{vmatrix}_{at(x_0, y_0)} < 0$$
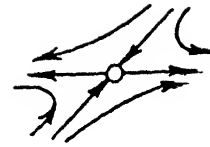
or it corresponds to one positive or negative eigen values. If $\Delta < 0$ and $J < 0 \Rightarrow$ saddle point of separation

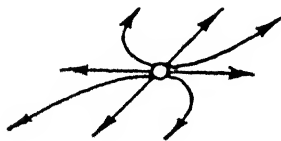if $\Delta > 0 \ and \ J < 0 \Rightarrow$ saddle point of attachment
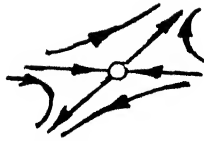
Saddle



Saddle

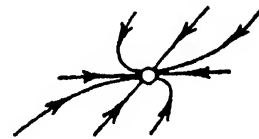Saddle point of separation

Saddle point of reattachment

**Nodal Points:** are the points through which an infinite number of shear stress lines pass. Nodal Points are of two types, regular nodal points (or nodes) and foci (or spiral nodes).

**Nodes**: Mathematically $J > 0$ for the nodal points



Source



Sink

$$J > 0, \Delta > 0, w < 0$$

$$J > 0, \Delta < 0, w > 0$$

The above two are regular nodes. For the stable node (sink), both the eigen values are negative. For the unstable node, both the eigen values are positive.

**Spiral node:** Here the skin friction lines spiral onto or out of this point. This correspond to complex eigen values. If the real part of the eigen value is negative it is a stable spiral and if the real part of the eigen value is positive, it corresponds to an unstable spiral.



Stable Spiral



Unstable Spiral